https://doi.org/10.1016/j.fuel.2019.115857

Numerical study on fractal-like soot aggregate dynamics of turbulent ethylene-oxygen flame

Shuyuan Liu[1], Tat Leung Chan[1,2*], Jianzhong Lin[3], Mingzhou Yu[4]

1. Department of Mechanical Engineering, The Hong Kong Polytechnic University, Kowloon, Hong Kong
2. The Hong Kong Polytechnic University, Shenzhen Research Institute, Shenzhen, PR China
3. Institute of Fluid Engineering, Zhejiang University, Hangzhou, Zhejiang, PR China
4. Department of Atmospheric Sciences, Zhejiang University, Hangzhou, Zhejiang, PR China

[*]Corresponding Author and E-mail: mmtlchan@polyu.edu.hk (T.L. Chan)

Abstract

The soot aggregate dynamics of turbulent ethylene-oxygen flame is numerically studied for different equivalence ratios and jet Reynolds numbers (Re_j). Our developed Taylor-series expansion method of moments (TEMOM) model in our previous research studies is further extended to solve the bivariate population balance equation (PBE) and formulate the novel Bivariate TEMOM model scheme. Full numerical validation are performed with the stochastically weighted operator splitting Monte Carlo method and moving sectional method, the Bivariate TEMOM model scheme coupled with large eddy simulation (LES) method and soot formation model is used to simulate fractal-like soot aggregate dynamics in turbulent ethylene-oxygen flame. The results show that soot nucleation and surface growth processes are enhanced with increasing equivalence ratio while the coagulation rate is hardly varied as the total soot volume fraction is quite low. The increasingly uniform distributions of fractal dimension and particle size can also be observed. As Re_j increases from 14,400 to 36,000, both the mean diameter and mean fractal dimension of soot aggregates gradually decrease as the surface growth rates of soot aggregates decrease significantly. However, the effect of increasing Re_j on coagulation and nucleation rates are slight due to the decreasing residence time of soot particles in the combustor.

Keywords: Turbulent flame; Fractal-like soot dynamics; Bivariate TEMOM; Large eddy simulation

1. Introduction

The combustion processes of carbon-containing fuels [1-7] contribute the major air pollutants (e.g. gaseous and particulate emissions) which have drawn increasing attention. Compared with gaseous emissions, the particulate emissions, i.e., soot particles with fractal-like geometry can significantly affect the radiation, structure and emission properties of combustion flames when carbon-containing fuels are burned [8-9]. Particle dynamics (e.g. collision induced aggregation nucleation and growth) plays an important role in the formation and evolution of particle size distribution (PSD) as well as characteristic morphology of fractal-like soot aggregate particles [9]. Generally, the structure of fractal-like soot aggregates can be described by the following relationship between the number of primary particles in the soot aggregates, n and the gyration radius, R_g [10-11],

$$n = k_g\left(\frac{2R_g}{d_0}\right)^{D_f} \tag{1}$$

where k_g is a pre-factor, D_f is the fractal dimension of soot aggregates, d_0 is the diameter of primary particles, R_g is the gyration radius of the fractal like soot aggregates. Eq. (1) shows that there exists a scale invariant relationship between the number of primary particles in the aggregate, n and the gyration radius, R_g, which had been verified by both experimental and numerical studies [12-17].

According to Xiong & Friedlander [18], interactions between particles of different morphologies described by their fractal dimensions can lead to distributions of particle morphologies for the same particle size. These interactions can take place due to the different particle formation and evolution histories as well as due to designed mixing of different particle populations. Examples include the natural interaction among soot particles in an internal combustion engine and the forced mixing of aerosol particles in an aerosol reactor [9]. Apart from the effect on particle morphology distributions of soot particles, the fractal dimension also affects coagulation dynamics between fractal-like soot aggregates. Mountain et al. [19] and Mulholland et al. [20] have demonstrated that the shape of self-preserving distribution depends significantly on the fractal dimensions of fractal-like soot aggregates. Therefore, both the aggregate size distribution (represented by the number of primary particles) and fractal dimension distribution should be taken into account in numerical simulations of fractal-like soot aggregates dynamics.

Since Friedlander [22] proposed the general population balance equation (PBE) for aerosol dynamics originating from the Smoluchowski [23] discrete coagulation equation, PBE has been the most widely used governing equations for mean field simulation of aerosol-related problems. Examples include atmospheric and industrial aerosols, colloidal and polymer sciences, powder technology etc. [21]. Considerable research studies on particle dynamics are carried out by many researchers [7,24-31] to overcome the complexity and difficulty in theoretical and experimental studies on PBE. Generally, PBE proposed by Friedlander [22] is adequate to describe typical aerosol dynamic processes including nucleation, condensation, and coagulation etc. taking place within simple particulate systems. The main feature of such systems is that only one variable i.e. particle size is needed to describe the particulate system completely. The popular numerical methods for the solution of PBE mainly include sectional methods [32-35], Monte Carlo methods [30,36-40], and moment methods [7,41-44]. On the other hand, the exact and analytical solutions of PBE can also be obtained by e.g., the group analysis [28,31] and the separate variable method [45]), respectively. As far as fractal aggregates are concerned, a modified coagulation kernel including a pre-specified fractal dimension for the entire aggregate population is often used due to the computing limitations [46]. However, the significant progress in computing power has made the solution of bivariate PBE possible so that a more realistic and accurate description of fractal aggregates can be obtained.

Among the numerous numerical methods to solve the population balance equation (PBE), Yu, Lin and Chan [42] firstly developed a novel Taylor-series expansion method of moments (TEMOM) for the solution of PBE. The TEMOM has been proven to be an effective and highly promising method of moments due to its inherent high accuracy and efficiency for univariate PBE [7,44-45,47-48]. Recently, TEMOM has been extended by Jiang et al. [49] to the two-component aggregation problem undergoing Brownian coagulation. The main novelty of the present study lies in that a Bivariate TEMOM (Biv-TEMOM) model scheme with consideration of both size and fractal dimension of soot aggregates is newly developed and coupled with large eddy simulation (LES) method as well as the detailed combustion chemistry and soot formation model to account for the fractal-like soot aggregates formed in the premixed flame of ethylene-oxygen. The formulated LES-Bivariate TEMOM model scheme is then applied to study the effects of equivalence ratio (ϕ) and jet Reynolds number (Re_j) which have significant impact of the formation and evolution of soot particles. The present study is aimed to provide a deeper insight into the formation and evolution mechanisms of fractal-like soot aggregates in turbulent combustion flows.

Nomenclature

A	area of computational element, m^2	$\dot{Q}_{\mathrm{ox}}$	volume flowrate of oxygen, m^3/s
A_k	model constant, 1.591	$\dot{Q}_{\mathrm{fuel}}$	volume flowrate of fuel, m^3/s
A_f	dimensionless restructuring parameter	Re_{j}	jet Reynolds number at nozzle exit
A_t	accommodation coefficient soot model	Rg	gyration radius of aggregates, nm
b	dimensionless model parameter	R_{restr}	restructuring rate of aggregate
B	collision frequency, #/s	S	surface area, m^2
c	post-collisional particle property	$\bar{S}_{ij}$	strain rate tensor
C	slip correction factor	S_φ, S_ψ	source term
C_n	nucleation rate constant, $\#/(m^3 \cdot s)$	t	time, s
C_1, C_2	soot oxidation rate constants	T	flame temperature, K
d_0	diameter of primary particles, nm	u	velocity, m/s
d	inner diameter of the nozzle in the combustor, m	v	particle volume, m^3
D_c	asymptotic fractal dimension of soot aggregates	v_c	collision volume of aggregates, m^3
D_f	fractal dimension of soot aggregates	z	post-collisional model parameter
D_m	mean fractal dimension of soot aggregates	*Greek letters*	
D_{p}	collision diameter of soot aggregates, nm	α	fraction of reaction sites available
D_r	asymptotic fractional dimension	β	collision kernel, $\#/(m^3 \cdot s)$
D_s	diffusion coefficient, m^2/s	γ	thermophoretic coffiecent
D_1, D_2	fractal dimensions of colliding partners	δ	Kronecker operator
f	inverse of D_f	$\varDelta_s$	mass change of particle, kg
$f(v,\varphi,t)$	dimensionless probability density function	$\zeta, \eta, \vartheta, \xi, \varsigma$	combination of moments
g	dimensionless restructuring parameter	μ	dynamic viscosity, $kg/(m \cdot s)$
G	Gibbs free energy, kJ/mol	ρ	density, kg/m^3
$G_{s,i}$	surface growth rate, $kg/m^3/s$	ρ_s	Soot density, kg/m^3
h	specific total enthalpy, J/mol	σ_{ij}	fluid shear stress tensor
J_0	homogeneous nucleation rate, $\#/(m^3 \cdot s)$	τ_{ij}	subgrid scale stress tensor
k_B	Boltzmann constant, J/K	τ	dimensionless time, s/s
k	moment order	φ	arbitrary physical variable
k_g	pre-factor in gyration relationship	ϕ	equivalence ratio of fuel to oxygen
K	coagulation kernel, $\#/(m^3 \cdot s)$	ψ	soot number or mass density
Kn	Knudsen number	$\varOmega$	soot oxidation rate, $kg/(kmol \cdot s)$
l	moment order	*Abbreviations*	
L	horizontal distance from the nozzle exit, m	Biv-TEMOM	bivariate Taylor-series expansion method of moments

$M_{k,l}$	bivariate moment of order k and l	FDD	fractal dimension distribution
M_{soot}	mass of a soot nucleus, kg/kmol	LES	large eddy simulation
M	soot mass density, kg/m^3 mixture	PBE	population balance equation
N	total number density of soot particles, #/m^3	EFPV	extended flamelet/progress variable
n	mean number of primaries per aggregate, #/#	PSD	particle size distribution

2. Numerical methodology

2.1.1. Gas phase model

The flame solver package OpenSMOKE used in our previous experimental and numerical studies [4] is used to simulate the gas phase reactions of the burner-stabilized premixed impinging flames. This solver is an open source framework for numerical simulations of with detailed kinetic mechanisms. The species diffusion is modeled using the mixture-averaged diffusion model while thermal diffusion is considered in the species transport equations. The detailed combustion mechanisms of methane and ethylene are based on a detailed description of the C1-C4 chemistry, which are fully validated against the experimental data in our previous study [4]. The mechanisms also account for the formation and disappearance of soot precursors including benzene, toluene and polycyclic aromatic hydrocarbons (PAH). Based on the finite volume method, the convection and diffusion terms are discretized by the second-order upwind scheme and the central difference scheme, respectively, and the coupling between velocity and pressure is completed by the pressure-implicit with splitting of operators (PISO) algorithm [1,4].

Large eddy simulation (LES) has been widely used to simulate nanoparticle-laden turbulent flows in our previous studies [7,50-51] due to its high computational accuracy with an acceptable computational efficiency resulting from the advancement of computing facilities. The main idea of LES is to split up the physical variables into two parts where the effects of large and small scale structures are respectively considered. In LES method, large scale structures are solved directly while the small scale structures are modeled by turbulence models. The governing equations of LES are obtained by filtering the Navier-Stokes equation, after which the filtered variables are defined as follows,

$$\overline{\varphi}(x, y, t) = \frac{1}{A}\int \varphi(x', y', t')\, dx'dy' \tag{2}$$

where φ is an arbitrary physical variable (e.g., species mass fraction, particle number concentration etc.), A is the area of the computational element, x and y are coordinate variables, t is time. Applying Eq. (2) to the Navier-Stokes equation and diffusion convection equation, the filtered equations can be obtained. The well known Smagorinsky-Lily model is used to model the subgrid stress. For details of the LES model can be found in our previous work [7].

2.1.2. Particulate phase

In order to account for fractal characteristics of fractal-like soot aggregates in combustion flows, a bivariate PBE with consideration for fractal dimension of soot aggregates is derived based on the developed bivariate population dynamics approach by Kostoglou et al. [21], the governing equation of particulate phase is as follows,

$$
\begin{aligned}
&\frac{\partial f(v,\varphi,t)}{\partial t}+\frac{\partial(\overline{u}_j f(v,\varphi,t))}{\partial x_j}-\frac{\partial}{\partial x_j}(D_s\frac{\partial f(v,\varphi,t)}{\partial x_j}) \\
&\quad =\frac{1}{2}\int_{\varphi 1}\int_{\varphi 2}\int_0^{\infty}\int_0^{\infty}K(v_1,v_2,\varphi_1,\varphi_2)\,\delta(v-c_v(v_1,v_2))\delta(\varphi-c_\varphi(\varphi_1,\varphi_2)) \\
&\quad \times f(v_1,\varphi_1,t)f(v_2,\varphi_2,t)\mathrm{d}v_1\mathrm{d}v_2\mathrm{d}\varphi_1\mathrm{d}\varphi_2 \\
&\quad -f(v,\varphi,t)\int_{\varphi_1}\int_0^{\infty}K(v,v_1,\varphi,\varphi_1)f(v_1,\varphi_1,t)\mathrm{d}v_1\mathrm{d}\varphi_1+\frac{\partial G(v,\varphi)f(v,\varphi,t)}{\partial\varphi} \qquad (3)
\end{aligned}
$$

where $f(v,\varphi,t)$ is the probability density function of particle number density in terms of particle volume, v and another variable, φ, D_s is the effective diffusion coefficient, $K(v_1,v_2,\varphi_1,\varphi_2)$ is the coagulation rate between particles (v_1,φ_1) and (v_2,φ_2), δ is the Dirac delta function and $G(v,\varphi)$ is the other dynamic process besides coagulation, which is nucleation process in the present study. The functions, c_v, c_φ are the values of v, φ for the new particle after the coagulation event. Generally, $c_v(v_1,v_2) = v_1+v_2$ due to the conservation of total particle volume. However, the relationship between c_φ and φ_1, φ_2 is dependent on the constitutive law of specific physical mechanism underlying the evolution of fractal dimension, φ, which may be surface growth or sintering processes etc.

In the present study, the constitutive law for post-collisional fractal dimension proposed by Kostoglou and Konstandopoulos [45] is used to further account for the fractal dimension evolution of fractal-like soot aggregates. This formalism was also used by di Stasio et al. [52] to describe the evolution of size and morphology of flame soot aggregate. After some modifications in order to reflect the assumptions and limitations of the measurement technique, the modified constitutive law for post-collisional fractal dimension of soot aggregates can be written as [21],

$$c(v_1,v_2,D_1,D_2) = \frac{D_c \ln[b(zv_1+zv_2)/v_0]}{\ln[b((zv_1/v_0)^{D_c/D_1}+(zv_2/v_0)^{D_c/D_2})]} \tag{4}$$

where v_0 is the volume of primary particles, v_1, v_2, D_1, D_2 are the volume and the fractal dimension of the two colliding aggregate particles, respectively, D_c is the asymptotic fractal dimension resulting from the coagulation between aggregate particles, b and z are the model parameters.

2.2. Soot formation model

The extended flamelet/progress variable (EFPV) approach in [53] is used in the present study. This modified combustion model includes detailed combustion chemistry and soot formation model. In order to model soot particles evolving from spherical to fractal shape, the simultaneous nucleation of primary particles, coagulation between primary and fractal particles, and the surface growth processes are considered in the present study.

2.2.1. Soot transport equation

The transport equations in terms of soot number density, N and soot mass density, M can be written as follows [53],

$$\frac{\partial(\rho\psi)}{\partial t}+\frac{\partial(\rho\overline{u}_j\psi)}{\partial x_j} = \frac{\partial}{\partial x_j}(\rho D_s\frac{\partial\psi}{\partial x_j})+\gamma\frac{\mu}{T}\psi\frac{\partial T}{\partial x_j}+S_\psi \tag{5a}$$

where

$$\gamma = \frac{3}{4(1+\pi A_t/8)} \tag{5b}$$

$$S_N = \frac{1}{N_A}[(\frac{dN}{dt})_{nucl}+(\frac{dN}{dt})_{coa}] \tag{5c}$$

$$S_M = \frac{M_{soot}}{N_A}[(\frac{dN}{dt})_{nucl}+(\frac{dM}{dt})_{grow}+(\frac{dM}{dt})_{oxi}] \tag{5d}$$

where the subscripts of nucl, coa, grow, oxi represent nucleation, coagulation, surface growth and oxidation processes, respectively. γ is related to the thermophoretic transport effect of soot particles, the accommodation coefficient, A_t is set to be 1.0. M_{soot} is the mass of a soot nucleus with a value of 1200 kg/kmol.

2.2.2. Soot aggregate coagulation kernels

With the increase of Knudsen number (Kn), the flow regimes can be classified into four regimes in coagulation process, i.e. continuum, Epstein, transition and molecular regimes.

(*i*) *Coagulation in continuum regime*

When Kn << 1, the flow regime falls into the continuum and near continuum regime (i.e., the Epstein regime). The coagulation kernel of these two flow regimes can be unified after introducing the following slip correction factor, which is valid for Kn up to 5 [54],

$$C(v_c) = 1 + A_k Kn \tag{6a}$$

where v_c is the collision volume of aggregates, A_k =1.591, $Kn = \lambda/r$ is the ratio of mean free path of gas to the particle radius. The coagulation kernel of fractal-like soot aggregates in continuum and Epstein coagulation [9,55] is written as,

$$\beta_c(v_1, v_2) = B_c(v_1^{1/D_1} + v_2^{1/D_2})\left(\frac{C(v_{c1})}{(v_{c1})^{1/D_1}} + \frac{C(v_{c2})}{(v_{c2})^{1/D_2}}\right) \tag{6b}$$

where $B_c = 2k_B T/3\mu$, v_c is the collision volume of aggregates, D_1, D_2 are the fractal dimension of the two colliding aggregate particles.

It is also noted that $n = v/v_0$, $v_c = v_0^{1-D_f/3} v^{D_f/3}$, where v, v_0 are the real volume of agglomerate, the volume of primary ,particles, respectively. Combining $n = v/v_0$, $v_c = v_0^{1-D_f/3} v^{D_f/3}$ with Eq. (1), the collision kernel of aggregates in continuum and near continuum regimes [7] can be expressed as,

$$\beta_c(v_1, v_2) = B_c\{(\frac{1}{v_1^f} + \frac{1}{v_2^f})(v_1^f + v_2^f) + \varphi_c v_0^{(f-1/3)}(\frac{1}{v_1^{2f}} + \frac{1}{v_2^{2f}})(v_1^f + v_2^f)\} \tag{7}$$

where $B_c = 2k_BT/3\mu$, k_B is the Boltzmann constant, μ is the viscosity of carrier gas, $f = 1/D_f$ where D_f is the geometric mean fractal dimension of the two colliding particles (i.e., $D_f = \sqrt{D_1D_2}$). $\varphi_c = 1.591\lambda/(3/4\pi)^{1/3}$ where λ is the mean free path of air molecular, and v_0 is the volume of primary particles.

(*ii*) *Coagulation in free molecule regime*

When Kn >>1, the flow regime is in the free molecule regime, the coagulation for fractal aggregates [20,55] is expressed as,

$$\beta_f(v_1,v_2) = B_f(v_1^f+v_2^f)^2\left(\frac{1}{v_1}+\frac{1}{v_2}\right)^{1/2} \tag{8}$$

where $B_f = 2.2(3k_BTd_0/\rho_0)^{1/2}$, k_B is the Boltzmann constant, T is the temperature, μ is the viscosity of fluid gas, ρ_0 is the density of primary particles, d_0 is the diameter of primary particles, the factor of 2.2 is taken into account for the increased collision cross-section due to van der Waals forces between the two colliding aggregate particles [56]. $f = 1/D_f$ where D_f is the geometric mean fractal dimension of the two colliding particles, i.e., $D_f = \sqrt{D_1D_2}$.

(*iii*) *Coagulation in transition regime*

For the transition flow regime, the harmonic mean of the continuum and free molecule coagulation kernels [57] are used as,

$$1/\beta_t(n_i,n_j) = 1/\beta_c(n_i,n_j)+1/\beta_f(n_i,n_j) \tag{9}$$

where $\beta_t(n_i,n_j)$ is the coagulation kernel in the transition regime.

2.2.3. Soot nucleation, surface growth and oxidation models

A well-known simplified soot inception model in [53] is used to calculate the soot nucleation rate. In this model, the soot inception is correlated with acetylene concentration and takes the form as,

$$J_0(t) = C_nN_A\left(\rho\frac{Y_{\text{acetylene}}}{W_{\text{acetylene}}}\right)\exp\left(-\frac{21{,}000}{T}\right) \tag{10}$$

where ΔG^* is the free energy that is required to form a stable nucleus and C_n is a constant, $54 s^{-1}$, N_A is Avagadro number, ρ is the mixture denstiy, T is the temperature, $Y_{\mathrm{acetylene}}$ and $W_{\mathrm{acetylene}}$ are the mass fraction and molecular weight of acetylene, respectively.

The surface growth term is modified based on the model of Kazakov and Frenkach [58],

$$G_{s,i} = k_s C_g \alpha \chi_s m_i \Delta_s S_i N_i \tag{11}$$

where $G_{s,i}$ is the surface growth rate of the i-th particle due to the surface chemical reactions of soot aggregates, k_s is the per-site rate coefficient, C_g is the concentration of gaseous species, α is the fraction of reaction sites available, χ_s is the number density of active surface sites, Δ_s is the mass change due to the surface growth, and m_i, S_i, N_i are the mass, surface area and number density of the i-th particle, respectively.

Considering the effect of both O_2 and OH radical, the soot oxidation rate in [53] is used in the present study,

$$\Omega_{\mathrm{oxi}} = -C_1 \frac{Y_{\mathrm{OH}}}{W_{\mathrm{OH}}} \rho T^{0.5} (\pi N)^{1/3} (6M/\rho_s)^{2/3} - C_2 \frac{Y_{\mathrm{O_2}}}{W_{\mathrm{O_2}}} \exp\left(-\frac{19{,}778}{T}\right) \rho T^{0.5} (\pi N)^{1/3} (6M/\rho_s)^{2/3} \tag{12}$$

where C_1, C_2 are constants and take the values of 13.7553 $\mathrm{kg \cdot m/(kmol \cdot K^{1/2} \cdot s)}$ and 8903.51 $\mathrm{kg \cdot m/(kmol \cdot K^{1/2} \cdot s)}$, respectively. Y and W are the mass fraction and molecular weight, respectively. N, M are the number and mass density of soot aggregate, respectively. ρ is the density of the mixture, ρ_s the density of soot aggregate and is set to be 2000 $\mathrm{kg/m^3}$.

2.3. Restructuring of fractal-like soot aggregates

Since the effect of restructuring on fractal dimension of soot aggregates at high temperature is significant, aggregate restructuring is considered. According to Kostoglou [21], the restructuring of soot aggregates can be treated as a sequence of restructuring events caused by the internal rearrangement of monomers of soot aggregates. Such restructuring process will eventually drive soot aggregates to have an asymptotically fractal dimension, D_r. If the simplest first-order relaxation of aggregates is considered, the restructuring rate takes the form as,

$$R_{restr} = \frac{1}{\tau_r}(D - D_r) \tag{13}$$

where τ_r is the relaxation time related to the restructuring on the time scale and size of fractal-like soot aggregates and takes the form as,

$$\tau_r = f(n, g) \tag{14}$$

where n is the number of primary particles in the aggregates, g is the parameter related to the restructuring on the time scale.

2.4. The moment equations

In order to transform Eq. (3), a bivariate moment of order, k and l with respect to particle volume and fractal dimension is defined as,

$$M_{k,l} = \int_0^\infty \int_0^\infty v^k \varphi^l f(v,\varphi,t)\mathrm{d}v\mathrm{d}\varphi \tag{15}$$

By multiplying Eq. (3) with $v^k\varphi^l$, and integrating over all particle size and fractal dimension, the time evolution equation of moments can be obtained,

$$\frac{dM_{k,l}}{dt} + \frac{\partial(\overline{u}_j M_{k,l})}{\partial x_j} - \frac{\partial}{\partial x_j}\left(D_s \frac{\partial M_{k,l}}{\partial x_j}\right) =$$

$$\frac{1}{2}\int_{\varphi_1}\int_{\varphi_2}\int_0^\infty\int_0^\infty [(v_1+v_2)^k c_\varphi(\varphi_1,\varphi_2)^l - v_1{}^k\varphi_1{}^l \text{-} v_2{}^k\varphi_2{}^l] K(v_1,v_2,\varphi_1,\varphi_2)$$

$$\times f(v_1,\varphi_1,t) f(v_2,\varphi_2,t)\mathrm{d}v_1\mathrm{d}v_2\mathrm{d}\varphi_1\mathrm{d}\varphi_2 + G(v)v^k \tag{16}$$

where D_s is the effective diffusion coefficient, $G(v)$ is the other particle dynamic processes (i.e., nucleation, surface growth) besides coagulation in the present study. In order to derive the expression of $M_{k,l}$ in terms of some base moments, $v^k\varphi^l$ is expanded in a binary Taylor-series at point ($v = v_m$, $\varphi = \varphi_m$), where $v_m = \frac{M_{1,0}}{M_{0,0}}$, $\varphi_m = \frac{M_{0,1}}{M_{0,0}}$, representing the mean volume and fractal dimension of soot aggregates, respectively. According to the L'Hospital's law , the convergence regime of the binary Taylor-series expansion of $v^k\varphi^l$ is $[0, 2v_m] \times [0, 2\varphi_m]$ [51]. Taking the first three orders, the binary Taylor-series expansion of $v^k\varphi^l$ can be written as,

$$v^k\varphi^l \cong v_m{}^k\varphi_m{}^l + v_m{}^k l\varphi_m{}^{l\text{-}1}(\varphi-\varphi_m) + \frac{1}{2}(l\text{-}1)lv_m{}^k\varphi_m{}^{l\text{-}2}(\varphi-\varphi_m)^2$$
$$+klv_m{}^{k\text{-}1}\varphi_m{}^{l\text{-}1}(v-v_m)(\varphi-\varphi_m) + \varphi_m{}^l kv_m{}^{k\text{-}1}(v-v_m) + \frac{1}{2}(k\text{-}1)kv_m{}^{k\text{-}2}\varphi_m{}^l(v-v_m)^2 \quad (17)$$

Substituting Eq. (17) into Eq. (15), Eq. (15) can then be rewritten as,

$$M_{k,l} = [(1+kl+\frac{k^2\text{-}3k+l^2\text{-}3l}{2})v_m{}^k\varphi_m{}^l]M_{0,0} + [(2k\text{-}k^2\text{-}kl)v_m{}^{k\text{-}1}\varphi_m{}^l]M_{1,0}$$
$$+[(2l\text{-}kl\text{-}l^2)v_m{}^k\varphi_m{}^{l\text{-}1}]M_{0,1} + kl\varphi_m{}^{l\text{-}1}v_m{}^{k\text{-}1}M_{1,1} + [(\frac{k^2\text{-}k}{2})v_m{}^{k\text{-}2}\varphi_m{}^l]M_{2,0} + [(\frac{l^2\text{-}l}{2})v_m{}^k\varphi_m{}^{l\text{-}2}]M_{0,2} \quad (18)$$

where $M_{0,0}$, $M_{1,0}$, $M_{0,1}$, $M_{1,1}$, $M_{2,0}$, $M_{0,2}$ are six base moments and can be used to express any order moments.

Substituting the continuum regime coagulation kernel in Eq. (7) to Eq. (16), the ordinary differential equations (ODEs) of the first three order moments can be expressed as,

$$\frac{dM_{0,0}}{dt} = -\frac{\partial(\overline{u}_j M_{0,0})}{\partial x_j} + \frac{\partial}{\partial x_j}\left(D_s\frac{\partial M_{0,0}}{\partial x_j}\right) - \frac{B_c}{2}(\xi_1 + \phi\, v_0{}^{(f\text{-}1/3)}\xi_2) + G(v)$$

$$\frac{dM_{1,0}}{dt} = -\frac{\partial(\overline{u}_j M_{1,0})}{\partial x_j} + \frac{\partial}{\partial x_j}\left(D_s\frac{\partial M_{1,0}}{\partial x_j}\right) + G(v)v$$

$$\frac{dM_{0,1}}{dt} = -\frac{\partial(\overline{u}_j M_{0,1})}{\partial x_j} + \frac{\partial}{\partial x_j}\left(D_s\frac{\partial M_{0,1}}{\partial x_j}\right) + \frac{B_c}{2}(\eta_1 + \phi\, v_0{}^{(f\text{-}1/3)}\eta_2) + G(v)$$

$$\frac{dM_{1,1}}{dt} = -\frac{\partial(\overline{u}_j M_{1,1})}{\partial x_j} + \frac{\partial}{\partial x_j}\left(D_s\frac{\partial M_{1,1}}{\partial x_j}\right) + \frac{B_c}{2}(\zeta_1 + \phi\, v_0{}^{(f\text{-}1/3)}\zeta_2) + G(v)v$$

$$\frac{dM_{2,0}}{dt} = -\frac{\partial(\overline{u}_j M_{2,0})}{\partial x_j} + \frac{\partial}{\partial x_j}\left(D_s\frac{\partial M_{2,0}}{\partial x_j}\right) + \frac{B_c}{2}(\varsigma_1 + \phi\, v_0{}^{(f\text{-}1/3)}\varsigma_2) + G(v)v^2$$

$$\frac{dM_{0,2}}{dt} = -\frac{\partial(\overline{u}_j M_{0,2})}{\partial x_j} + \frac{\partial}{\partial x_j}\left(D_s\frac{\partial M_{0,2}}{\partial x_j}\right) + \frac{B_c}{2}(\vartheta_1 + \phi\, v_0{}^{(f\text{-}1/3)}\vartheta_2) + G(v) \quad (19)$$

where

$$\xi_1 = 2M_{0,0}M_{0,0} + M_{f,0}M_{\text{-}f,0} + M_{\text{-}f,0}M_{f,0}$$

$$\xi_2 = M_{0,0}M_{\text{-}f,0} + M_{f,0}\,M_{\text{-}2f,0} + M_{f,0}\,M_{\text{-}2f,0} + M_{0,0}M_{\text{-}f,0}$$

$$\eta_1 = 2M_{0,1/2}M_{0,1/2} + M_{f,1/2}M_{\text{-}f,1/2} + M_{\text{-}f,1/2}M_{f,1/2} - 4M_{0,1}M_{0,0} - 2M_{\text{-}f,1}M_{0,f}$$

$$\eta_2 = M_{\text{-}f,1/2}M_{0,1/2} + M_{f,1/2}M_{\text{-}2f,1/2} + M_{\text{-}2f,1/2}M_{f,1/2} + M_{0,1/2}M_{\text{-}f,1/2} - 2M_{\text{-}f,1}M_{0,0} - 4M_{f,1}M_{\text{-}2f,0}$$
$$-2M_{\text{-}f,1}M_{0,0}$$

$$\zeta_1 = 4M_{1,1/2}M_{0,1/2}+2M_{1\text{-}f,1/2}M_{f,1/2}+2M_{1+f,1/2}M_{\text{-}f,1/2} - 4M_{1,1}M_{0,0} - 2M_{1\text{-}f,1}M_{0,0} - 2M_{1+f,1}M_{\text{-}f,0}$$

$$\zeta_2 = 2M_{1\text{-}f,1/2}M_{0,1/2}+2M_{1\text{-}2f,1/2}M_{f,1/2}+2M_{1+f,1/2}M_{\text{-}2f,1/2}+2M_{1,1/2}M_{\text{-}f,1/2} - 2M_{1\text{-}f,1}M_{0,0}$$
$$-2M_{1\text{-}2f,1}M_{f,0} - 2M_{1+f,1}M_{\text{-}2f,0} - 2M_{1,1}M_{\text{-}f,0}$$

$$\varsigma_1 = 4M_{1,0}M_{1,0}+4M_{1\text{-}f,0}M_{1+f,0}$$

$$\varsigma_2 = 4M_{1\text{-}f,0}M_{1,0}+4M_{1\text{-}2f,0}M_{1+f,0}$$

$$\vartheta_1 = 2M_{0,1}M_{0,1}+2M_{f,1}M_{\text{-}f,1} - 4M_{0,2}M_{0,0} - 2M_{\text{-}f,2}M_{f,0} - 2M_{f,2}M_{\text{-}f,0}$$

$$\vartheta_2 = 2M_{\text{-}f,1}M_{0,1}+2M_{f,1}M_{\text{-}2f,1} - 2M_{\text{-}f,2}M_{0,0} - 2M_{\text{-}2f,2}M_{f,0} - 2M_{f,2}M_{\text{-}2f,0} - 2M_{0,2}M_{\text{-}f,0} \tag{20}$$

It can be seen that there are still fractional-order moments in Eq. (20). In order to achieved moment equations closure, substituting Eq. (18) into Eq. (20), the fractional-order moments can be expressed in terms of the six base moments (i.e., $M_{0,0}$, $M_{1,0}$, $M_{0,1}$, $M_{1,1}$, $M_{2,0}$, $M_{0,2}$). Take the fractional-order moment, $M_{f,0}$ for an example, let $k = f$, $l = 0$, then $M_{f,0}$ can be expressed as,

$$M_{f,0} = \left(\frac{2+f^2\text{-}3f}{2}\right)v_m^{\,f}M_{0,0}+(2f\text{-}f^2)\, v_m^{\,f\text{-}1}M_{1,0}+\left(\frac{f^2\text{-}f}{2}\right)v_m^{\,f\text{-}1}M_{2,0} \tag{21}$$

All the other fractional-order moments can also be expressed with the six base moments. Now, the only unclosed terms in Eq. (16) are the term $G(v)$, which accounts for nucleation and surface growth. For the homogeneous nucleation process, the nucleation rate in Eq. (10) takes the nucleation rate [59], which accounts for the fractal-like soot particle nucleation process. For the surface growth rate in Eq. (11), it can be determined by using the combustion and soot surface reaction mechanism [60]. Therefore, Eq. (19) is now automatically closed without any priori assumption for PSD.

In order to reduce the numerical uncertainty caused by the huge difference in values of traced moments, a non-dimensionalization method [7] is used. The moment $M_{k,l}$ and the reaction rate due to nucleation and surface growth are non-dimensionalized as follows,

$$M^*_{k,l} = \frac{M_{k,l}}{N_r v_0^{\,k} D_r^{\,l}} \tag{22}$$

$$G^*(v,\varphi) = \frac{G(v,\varphi)}{N_r/\tau} \tag{23}$$

where N_r is the reference soot particle number density which is a typical flame soot number density of 1×10^{13} #/cm^3 used in [58]. v_0 is the volume of primary particles, D_r is the reference fractal dimension [8,58]. τ is the dimensionless time scale. For the free molecule regime coagulation and transition regime coagulation, the transformed moment equations accounting for coagulation and other dynamic processes and transport terms of fractal aggregates can be derived in a similar way to the above derivation process.

2.5. Simulation setup

A similar cylindrical combustor with radius of 0.225 m and length of 2 m shown in Fig. 1(a) [29] is used in the present study. A nozzle with diameter, d of 0.01 m and length of 0.01 m is located at the center of the cylindrical combustor. Three partitions with height of 0.05 m and thickness of 0.0005 m are evenly mounted in the axial direction inside the cylindrical aerosol reactor in order to enhance mixing process. Grid independence is tested by performing several different sets of grid meshes (i.e., 160×40, 160×50, 160×60, 150×60). The relative errors among these mesh systems were less than 1%. The grid meshes with 160×50 could satisfy the requirements of present study when considering both computational accuracy and efficiency. Due to the axisymmertrical configuration of the studied cylindrical combustor, a two-dimensional axisymmetric unstructured grid mesh 160×50 shown in Fig. 1(b) is used in the present study. The grid near the nozzle zone and internals is refined. The jet Reynolds number at the nozzle exit, Re_{j} is varied from 14,400 to 36,000 by increasing jet velocity of ethylene-oxygen binary mixture from 24 m/s to 60 m/s, respectively. The fuel to oxidant equivalence ratio, ϕ is defined as,

$$\phi = \frac{\dot{Q}_{\mathrm{fuel}}/\dot{Q}_{\mathrm{ox}}}{(\dot{Q}_{\mathrm{fuel}}/\dot{Q}_{\mathrm{ox}})_{\mathrm{stoich}}} \tag{24}$$

where $\dot{Q}_{\mathrm{fuel}}$, $\dot{Q}_{\mathrm{ox}}$ are the volume flow rates of fuel (i.e., ethylene in the present study) and oxidant, ox (i.e., oxygen, O_2), respectively. The subscript, stoich means the stoichiometric ratio of the combustion reaction between fuel and the oxidant. In the present study, ϕ are used from 1.5 to 2.0.

Fig. 1. Schematic configuration of the cylindrical combustor [29]: (a) three-dimensional combustor; (b) two-dimensional axisymmetric grid mesh.

2.6. Model validation

In the present study, the newly developed Bivariate TEMOM (Biv-TEMOM) model scheme is first used to study the coagulation and sintering processes of titanium dioxide aggregates. The initial conditions of the simulated case are shown in Table 1 [61]. The numerical simulation results obtained by the Biv-TEMOM model scheme are compared with the results obtained by our recently developed stochastically weighted operator splitting Monte Carlo (SWOSMC) method in Liu et al. [4] and the moving sectional method (MSM) developed by Tsantilis et al. [33]. Fig. 2 shows the numerical simulation results of aggregate coagulation and sintering processes under different residence times and temperatures. Fig. 2a shows the variation of the non-dimensional total aggregate particle number density, N/N_0 with residence time. The total aggregate number density is non-dimensionalized by the initial aggregate particle number density. With the increase of residence time, the total number density of aggregate particle decreases due to coagulation process for both temperatures. However, the total number density decreases faster for $T = 1073$K than that for T=1273K. This is because the collision cross sections of aggregates are reduced due to the sintering at high temperature [61]. Excellent agreement is found between the present numerical simulation results and Tsantilis et al. [33]. The mean diameter of primary particles, d_p is shown in Fig. 2b. As both coagulation and sintering results in the increase of particle size, the mean diameter of primary particles increases with residence time as well as reaction temperature. The numerical simulation results of mean primary particle diameter obtained by the Biv-TEMOM model scheme also agrees well with the numerical simulation results obtained by Liu et al. [4] and Tsantilis et al. [33]. Fig. 2c shows the variation of mean number of primary particles per aggregate, n_p with the residence time and temperature, respectively. With the increase of residence time, the mean number of primary particles per aggregate increases resulting from coagulation process. The mean number of primary particles per aggregate is significantly higher at $T = 1073$K than that at $T = 1273$K, which indicates that the degree of aggregation is higher when sintering rate is lower. The numerical simulation results are also consistent with the conclusion drawn by Kruis et al. [61] and Tsantilis et al. [33]. The results in Fig. 2 provides a preliminary and an excellent numerical validation for this developed Biv-TEMOM model.

Table 1 Initial conditions for model validation [61].

Fig. 2. Model validation with the stochastically weighted operator splitting Monte Carlo (SWOSMC) method [4] and the moving sectional method (MSM) [33]: (a) non-dimensional total number density of aggregate particles; (b) mean diameter of primary particles; and (c) mean number of primary particles per aggregate.

3. Results and discussion

This developed Bivariate TEMOM is further coupled with LES to simulate fractal-like soot aggregate dynamics in combustion flame of ethylene-oxygen and investigate the impact of equivalence ratio and inlet flow Reynolds number, Re_j. The simulated cases are listed in Table 2.

Table 2 Simulated cases of turbulent ethylene-oxygen flame.

3.1. The effect of different equivalence ratios (ϕ)

In order to study the soot aggregate dynamics in a high turbulent combustion flow, a typical Re_j = 36,000 (i.e., the nozzle exit velocity = 60 m/s) in turbulent ethylene combustion flow [62] is used for different ϕ in the present study. The effect of different Re_j on soot aggregate dynamics can be referred to Section 3.2. Fig. 3 shows the distributions of total volume fraction of soot aggregates along the axial distance for different equivalence ratios, ϕ at Re_j = 36,000. With the increase of ϕ, more soot nucleus are generated, thus the total volume fraction of soot aggregates increases significantly. It can also be found that soot aggregates mainly concentrate in the middle of the combustor. This may be explained by the rates of soot coagulation and nucleation distributions shown in Figs. 4 and 5, which also observe the highest values at the near middle region of the combustor. The large number of soot nucleus and particles concentrating in this region therefore leads to increasing total volume fraction. Figs 4 also shows that soot coagulation rate is not sensitive to ϕ in these specific cases. Although the increasing ϕ results in the increase of total soot volume fraction, the order of magnitude of total soot volume fraction is too small (~1×10^{-7} m^3/m^3) to cause any significant impact on coagulation process. In addition, coagulation and nucleation rates are also found the similar distributions as shown in Figs. 4 and 5 in the combustor. This may be because the formation and distribution of soot particles are greatly affected by the fluid phase of gaseous mixture as the inlet jet velocity is as high as 60 m/s when Re_j is 36,000.

Fig. 3. The total soot volume fraction (m^3/m^3) distributions along the axial distance (m) at $Re_j = 36{,}000$.

Fig. 4. The soot coagulation rate ($\times 10^{18}$ #/m^3/s) distributions along the axial distance (m) at $Re_j = 36{,}000$.

Fig. 5. The soot nucleation rate ($\times 10^{18}$ #/m^3/s) distributions along the axial distance (m) at $Re_j = 36{,}000$.

Fig. 6 shows that the distributions of surface growth rate of soot particles along the axial distance increases with increasing equivalence ratios, ϕ at $Re_j = 36{,}000$. Moreover, similar distributions can be found between Fig. 3 and Fig. 6, i.e. both the soot particles and surface growth reaction concentrate at the middle region of the combustor. This indicates that the surface growth rate is highly related to the total soot volume fraction. In fact, as more soot nucleus are generated at larger ϕ, they provide more surface and reaction sites available for surface growth process in Eq. (11). Therefore, the surface growth rate increases significantly with increasing ϕ. Fig. 7(a) shows the flame temperature distributions along the axial distance for different equivalence ratios, ϕ at $Re_j = 36{,}000$. With the increase of ϕ, flame temperature increases as more heat is released from the combustion reaction. The flame temperatures along the axial distance (m) at radial distance, $y = 0.05$ m are shown in Fig. 7(b). On the other hand, Fig. 7(b) shows that more obvious effect of ϕ on flame temperature distributions can be observed in the near-entrance and near-exit regions of the combustor. Flame temperature distributions are more uniform in the core region of the flame jet. This may be because the combustion flow is fully developed in the core region of the flame jet. In Fig. 7, the flame temperature distribution profiles are also consistent with the fractal-like soot aggregate dynamics as shown in Figs. 4 to 6. As the combustion takes place between ethylene and oxygen, heat is released from the combustion reaction along the axial jet flame flow direction of combustor. Therefore, flame temperature increases significantly within the potential core of jet flame. The thermal boundary layer is effectively suppressed by the internal partitions mounted inside the combustor, which is demonstrated by the flame temperature distributions at the near-middle region of the combustor.

Fig. 6. The soot surface growth rate ($kg/m^3/s$) distributions along the axial distance (m) at $Re_j = 36,000$.

Fig. 7. The effect of equivalence ratio, ϕ on flame temperature (K) at $Re_j = 36,000$: (a) flame temperature distributions and (b) flame temperatures along the axial distance (m) at radial distance, $y = 0.05$ m.

Fig. 8 shows the normalized particle size distributions (PSDs) for different ϕ and L/d at $Re_j = 36,000$, where L/d is the ratio of the horizontal distance from the nozzle exit, L to the nozzle diameter, d. As shown in Fig. 8(a), the PSDs of soot aggregates vary significantly for different L/d ratios when $\phi = 1.5$ and L/d, where L/d is the ratio of the axial distance from the nozzle exit, L to nozzle diameter, d. With the increase of L/d, the mean diameter of soot aggregate increases while the number density decreases due to coagulation process along the jet flow direction of combustor. With ϕ increasing from 1.5 to 1.6, the mean diameter of soot aggregate at $L/d = 110$ increases slightly from 210 nm to 225 nm. When ϕ increases from 1.6 to 2.0, the mean diameter of soot aggregates further increases to almost 300 nm. However, the difference among the PSDs for different L/d ratios decreases significantly when ϕ reaches at 1.8 or above. This may be because the axial jet mixing flow at high ϕ is enhanced, which reduces the difference of PSD for different L/d ratios. Fig. 9 shows the evolution of normalized soot aggregate fractal dimension distributions (FDDs) for different ϕ. As ϕ increases from 1.5 to 2.0, the mean fractal dimension of soot aggregates decreases significantly while the number density increases. This implies that aggregation that forms the fractal-like soot aggregates is enhanced as ϕ increases. In the present study, the asymptotic fractal dimension, D_c resulting from the coagulation between aggregate particles is set as 1.8 for Fig. 9 according to the numerical study on coagulation-dominant fractal particle dynamics in [21]. Since the coagulation and surface growth processes are not very significant (as shown in Figs. 4 and 6) in the present study, the fractal dimensions of a large number of newly formed soot nucleus are hardly varied by coagulation and surface growth processes. Therefore, the large number of soot nucleus with homogeneous size can be considered as monomers. With the increase of equivalence ratio from 1.5 to 2.0, the total volume fraction of soot particles significantly increases as shown in Fig. 3 which leads to the increase of total soot number density. The increase of total soot number density provides an increasing number of soot nucleus. According to the discussion of results obtained in [21], if more soot particle nucleus is introduced, the fractal dimension distribution (FDD) will be narrower and higher because soot particles are likely to reach the asymptotic distribution. The results obtained in the present study is also consistent with those obtained in [21]. The polydispersity of fractional dimension of soot aggregates also decreases with increasing ϕ which are reflected by the higher and narrower shape of FDD.

Fig. 8. The normalized particle size distributions of soot aggregates for different ϕ and *L/d* at Re_j = 36,000.

Fig. 9. The normalized fractal dimension distributions of soot aggregates for different ϕ at Re_j = 36,000.

3.2. The effect of different jet Reynolds numbers (Re_j)

Fig. 10 shows the total volume fractions of soot aggregates along the axial distance for different Re_j at ϕ = 1.5 which is a very typical equivalence ratio in ethylene-oxygen combustion and the results in Figs. 3 to 8 also show that the most significant difference of PSD appears at ϕ = 1.5. As Re_j increases, the total volume of soot aggregates decreases rapidly. This is because the residence time in the combustor is reduced due to increasing jet velocity. Therefore, less soot nucleus is formed with increasing Re_j. It can also be found that the soot aggregates concentrate at near the middle region of the combustor, which is similar to the results shown in Fig. 3. Fig. 11 shows the soot coagulation rate is not sensitive to the increase of Re_j. It may be because of the total volume fraction of soot aggregates is still so small (~1×10^{-6} m^3/m^3) as shown in Fig. 10 that coagulation events is not a dominant process. In Fig. 12, the soot nucleation rate, however, increases significantly with the increase of Re_j. According to our previous study of simultaneous coagulation and nucleation in turbulent flows [29], the higher Re_j may cause the delay of turbulent mixing so that nucleation becomes the dominant process in the potential core of the jet flow. Moreover, similar distribution profiles along the axial distance can also be found in Figs. 11 and 12, which suggests that coagulation and nucleation processes are basically controlled by fluid phase of gaseous mixture at high jet velocity.

Fig. 10. The total soot volume fraction (m^3/m^3) distributions along the axial distance (m) at ϕ = 1.5.

Fig. 11. The soot coagulation rate ($\times10^{18}$ $\#/m^3/s$) distributions along the axial distance (m) at ϕ = 1.5.

Fig. 12. The soot nucleation rate ($\times10^{18}$ $\#/m^3/s$) distributions along the axial distance (m) at ϕ = 1.5.

Fig. 13 shows the distributions of surface growth rate along the axial distance for different Re_{j} at ϕ = 1.5. With the increase of Re_{j}, the soot surface growth rate decreases rapidly. This is also because of the decreasing residence time in the combustor, which provides less surface sites and reaction sites available as well as less reaction time for the surface growth process. In Fig. 13, the soot surface growth process reaches the highest rate at near the middle region of combustor. Compared with the results in Fig. 10, it can be found that soot surface growth rate is highly dependent on total soot volume fraction distribution, which is consistent with the results shown in Figs. 3 and 6. Fig. 14 shows that with the increase of Re_{j}, the jet potential core increases greatly, which account for the increasing soot nucleation rate as shown in Fig. 12. The increasing flame velocity also results in shorter residence time within the combustor. It is also noteworthy that the flame velocity distribution shows obvious a two-dimensional stratification between the first and third partitions mounted inside the combustor. The velocity stratification is consistent with the stratification of coagulation, nucleation and surface growth rates as shown in Figs. 11 to 13.

Fig. 13. The soot surface growth rate (kg/m^3/s) distributions along the axial distance (m) at ϕ = 1.5.

Fig. 14. The flame jet velocity (m/s) distributions along the axial distance (m) at ϕ = 1.5.

Fig. 15 shows the variations of normalized particle size distributions (PSDs) of soot aggregates for different Re_{j}. As nucleation becomes a dominant process with the increase of Re_{j} from 14,400 to 36,000, the mean soot diameter decreases significantly from 250 nm to 150 nm at L/d = 100. Meanwhile, the normalized number density increases from 0.5 to 1.3 at L/d = 100 when Re_{j} increase from 14,400 to 36,000. Similar the variations of PSD can also be found for other L/d ratios with the increase of Re_{j}. As mentioned above, the increasing Re_{j} results in increasing jet velocity stratification, which in turn causes PSD stratification phenomenon for different L/d ratios. Therefore, the variations of PSD for different L/d ratios in Fig. 15 differ greatly from each other. Fig. 16 shows the variations of FDD for different Re_{j}. With the increase of Re_{j}, the residence time within the combustor significantly decreases so that the aggregation process that forms fractal-like aggregates is weakened. Therefore, the mean fractal dimension increases with Re_{j}. The polydispersity of fractional dimension of soot aggregates, however, increases with ϕ which is reflected by the lower but wider shape of FDD. The effect of jet Reynolds numbers, Re_{j} on the flame temperature distributions and flame temperatures along the axial distance are shown in Figs. 17(a) and (b), respectively. Fig. 17(a) shows the flame temperature distributions decrease with increasing Re_j in the near-nozzle region along the axial distance of jet flame from 0 to 1 m. This is because the jet velocity of the unburnt gas mixtures (ethylene-oxygen) is high at the exit of the nozzle. Fig. 17(b) shows that more obvious effect of Re_j on the flame temperatures can be observed at the near-nozzle region along the axial distance of jet flame from 0 to 1.0 m. The large amount of unburnt gas mixtures and the high jet velocity have the cooling effect at the near-nozzle region. With the increasing axial distance of jet flame to larger than 1.0 m, the flame temperature is dominated by the heat released from the combustion reaction. When ϕ is fixed, combustion reaction is not significantly affected by the highly turbulent combustion flow in the present study. Flame temperature distribution is only slightly affected by increasing Re_j. Therefore, the flame temperature distribution is hardly varied in the second half of the combustor (i.e., the axial distance of jet flame which is larger than 1.0 m).

Fig. 15. The normalized particle size distributions of soot aggregates for different Re_j at ϕ = 1.5.

Fig. 16. The normalized fractal dimension distributions of soot aggregates for different Re_j at ϕ = 1.5.

Fig. 17. The effect of jet Reynolds number, Re_j on flame temperature (K) at ϕ= 1.5: (a) flame temperature distributions and (b) flame temperatures along the axial distance (m) at radial distance, y = 0.05 m.

4. Conclusions

A coupled LES-Bivariate TEMOM model scheme is newly developed to simulate fractal-like soot aggregate dynamics in turbulent ethylene-oxygen combustion flows. This newly developed novel model scheme is fully validated with our recently developed stochastically weighted operator splitting Monte Carlo (SWOSMC) method in Liu et al. [4] and the moving sectional method (MSM) in Tsantilis et al. [33] with excellent agreement. This novel model scheme is then used to capture simultaneously the distributions of soot particle size and fractal dimension in turbulent combustion flows under the effects of equivalence ratio, ϕ and jet Reynolds number, Re_j. The main conclusions in the present study are as follows:

1. The results show the distinctly different effects of equivalence ratio and jet Reynolds number, Re_j on particle size distributions (PSDs) and fractal dimension distributions (FDDs) of soot particles. The

increase of equivalence ratio (ϕ), results in more uniform PSDs along the centerline of jet flame flow but narrower and higher fractal dimension distributions (FDDs) of soot particles. However, the increase of Re_j results in higher and broader PSDs but broader and lower FDDs.

2. The results reveal that both coagulation and nucleation rates have similar distribution patterns in heavily sooting and highly turbulent combustion flames. Similar distribution patterns can also be observed for the soot surface growth rate and total volume fraction of soot particles.
3. These results show that the mixing of soot precursors and soot particles becomes the dominant factor in the present highly turbulent combustion flows generated from the nozzle exit. These new findings provide new insight into the soot aggregate dynamics in heavily sooting flames and highly turbulent combustion flows.
4. These results demonstrate that this newly developed novel Bivariate TEMOM model scheme is capable of solving bivariate population balance equation (PBE) with high robustness. It can provide a deeper insight into the formation and evolution mechanisms of fractal-like soot aggregates in turbulent ethylene-oxygen flame.

Acknowledgements

The development of this novel Bivariate TEMOM model scheme was supported by the grants from the General Research Fund, Research Grants Council of the Hong Kong Special Administrative Region, China (Project No. PolyU 152125/15E) and the Central Research Grant of The Hong Kong Polytechnic University (Project No. B-Q47Y). The numerical verification with novel Monte Carlo method and previous soot dynamics model were supported by the grants from the National Natural Science Foundation of China (Project No. 11572274), and the Central Research Grant (Project No. 4-BCD3) and Mechanical Engineering Department (Project No. 88Y9) of The Hong Kong Polytechnic University.

References

[1] Z.L. Wei, H.S. Zhen, C.W. Leung, C.S. Cheung, Z.H. Huang, Experimental and numerical study on the emission characteristics of laminar premixed biogas-hydrogen impinging flame, Fuel 195(2017) 1-11.

[2] Z. Si, N. Shimasaki, K. Nishida, Y. Ogata, M. Guo, C.L. Tang, Z.H. Huang, Experimental study on impingement spray and near-field spray characteristics under high-pressure cross-flow conditions, Fuel 218(2018) 12-22.

[3] W. Zhang, J. Wang, Q. Yu, J. Wu, Z, Meng, Z.H. Huang, Investigation of the fuel effects on burning velocity and flame structure of turbulent premixed flames based on leading points concept, Combust. Sci. Technol. 11(2018) 1-23.
[4] S.Y. Liu, T.L. Chan, Z. He, Y.Y. Lu, X. Jiang, F.Z. Wei, Soot formation and evolution characteristics in premixed methane/ethylene-oxygen-argon burner-stabilized stagnation flames, Fuel 242(2019) 871-882.
[5] S. Guo, J. Wang, X. Wei, S. Yu, M. Zhang, Z.H. Huang, Numerical simulation of premixed combustion using the modified dynamic thickened flame model coupled with multi-step reaction mechanism, Fuel 233 (2018) 346–353.
[6] X.G. Wang, Z.H. Huang, W. Zhang, O.A. Kuti, K. Nishida, Effects of ultra-high injection pressure and micro-hole nozzle on flame structure and soot formation of impinging diesel spray, Appl. Energ. 88(2011) 1620-1628.
[7] T.L. Chan, S.Y. Liu, Y. Yue, Nanoparticle formation and growth in turbulent flows using the bimodal TEMOM, Powder Technol. 323(2018) 507-517.
[8] Z.L. Wei, C.W. Leung, C.S. Cheung, Z.H. Huang, Effects of H_2 and CO_2 addition on the heat transfer characteristics of laminar premixed biogas-hydrogen Bunsen flame, Int. J. Heat Mass Tran. 98(2016) 359-366.
[9] M.M. Maricq, Coagulation dynamics of fractal-like soot aggregates, J. Aerosol Sci. 38(2007) 141-156.
[10] S.R. Forrest, T.A. Witten, Long-range correlations in smoke-particle aggregates, J. Phys. A 12(1979) L109-L117
[11] R. Jullien, R. Botet, Aggregation and fractal aggregates. Singapore: World Scientific, 1987.
[12] R.A. Dobbins, C.M. Megaridis, Morphology of flame-generated soot as determined by thermophoretic sampling, Langmuir 3(1987) 254-259.
[13] C.M. Sorensen, Light scattering by fractal aggregates: A review, Aerosol Sci. Technol. 35(2001) 648-687.
[14] C.M. Sorensen, Scattering and absorption of light by particles and aggregates, In K.S. Birdi (Ed.), Handbook of surface and colloid chemistry (2nd ed), Boca Raton, FL: CRC Press, 2003.
[15] P. Meakin, Formation of fractal clusters and networks by irreversible diffusion limited aggregation, Phys. Rev. Lett. 51(1983) 1119-1122.
[16] P. Meakin, Universality, nonuniversality, and the effects of anisotropy on diffusion-limited aggregation. Phys. Rev. A 33(1986) 3371-3382.
[17] T.A. Witten, L.M. Sander, Diffusion limited aggregation, a kinetic critical phenomenon, Phys. Rev. Lett. 47(1981) 1400-1403.
[18] C. Xiong, S.K. Friedlander, Morphological properties of atmospheric aerosol aggregates, P. Natl. Acad. Sci. USA 98(2001) 11851-11856.
[19] R.D. Mountain, G.W. Mulholland, H. Baum, Simulation of aerosol agglomeration in the free molecular and continuum flow regimes, J. Colloid Interface Sci. 114(1986) 67-81.
[20] G.W. Mulholland, R.J. Samson, R.D. Mountain, M.H. Ernst, Cluster size distribution for free molecular agglomeration, Energ. Fuel. 2(1988) 481-486.
[21] M. Kostoglou, A.G. Konstandopoulos, & S.K. Friedlander, Bivariate population dynamics simulation of fractal aerosol aggregate coagulation and restructuring, J. Aerosol Sci. 37(2006) 1102-1115.
[22] S.K. Friedlander, Smoke dust and haze: Fundamentals of Aerosol Dynamics, NewYork: Wiley Interscience, 1977.
[23] M. Smoluchowski, Mathematical theory of the kinetics of the coagulation of colloidal solutions, Z. Phys. Chem. 19(1917) 129-135.
[24] W.C. Reade, L.R. Collins, A numerical study of the particle size distribution of an aerosol undergoing turbulent coagulation, J. Fluid Mech. 415(2000) 45-64.
[25] F. Guiaş, A stochastic approach for simulating spatially inhomogeneous coagulation dynamics in the gelation regime, Commun. Nonlinear Sci. Numer. Simulat. 14(2009) 204-222.
[26] S. Balachandar, J.K. Eaton, Turbulent dispersed multiphase flow, Annu. Rev. Fluid. Mech. 42(2010) 111-133.
[27] P. Zamankhan, Simulations of collision of ice particles, Commun. Nonlinear. Sci. Numer. Simulat. 15(2010) 1538-1552.
[28] A. Hasseine, H.J. Bart, A domain decomposition method solution of population balance equations for aggregation, nucleation, growth and breakup processes, Appl. Math. Model. 39(2014) 1975-1984.

[29] S.Y. Liu, T.L. Chan, A coupled CFD-Monte Carlo method for aerosol dynamics in turbulent flows, Aerosol Sci. Technol. 51(2017b) 269-281.
[30] S.Y. Liu, T.L. Chan, A stochastically weighted operator splitting Monte Carlo (SWOSMC) method for the numerical simulation of complex aerosol dynamic processes. Int. J. Numer. Method. H. 27(2017a) 263-278.
[31] F. Lin, S.V. Meleshko, A.E. Flood, Exact solutions of the population balance equation including particle transport, using group analysis, Commun. Nonlinear Sci. Numer. Simulat. 59(2018) 255-271.
[32] F. Gelbard, Y. Tambour, J.H. Seinfeld, Sectional representations for simulating aerosol dynamics, J. Colloid Interf. Sci. 76(1980) 541-556.
[33] S. Tsantilis, H.K. Kammler, S.E. Pratsinis, Population balance modeling of flame synthesis of titania nanoparticles, Chem. Eng. Sci. 57(2002) 2139-2156.
[34] S. Anand, Y.S. Mayya, M. Yu, M. Seipenbusch, G. Kasper, A numerical study of coagulation of nanoparticle aerosols injected continuously into a large, well stirred chamber, J. Aerosol Sci. 52(2012) 18-32.
[35] D. Mitrakos, E. Hinis, C. Housiadas, Sectional modeling of aerosol dynamics in multi-dimensional flows, Aerosol Sci. Technol. 41(2007) 1076-1088.
[36] D.T. Gillespie, Stochastic coalescence model for cloud droplet growth, J. Atmos. Sci. 29(1972) 1496-1510.
[37] R.I.A. Patterson, W. Wagner, M. Kraft, Stochastic weighted particle methods for population balance equations, J. Comput. Phys. 230(2011) 7456-7472.
[38] H. Zhao, C. Zheng, A population balance-Monte Carlo method for particle coagulation in spatially inhomogeneous systems, Comput. Fluids 71(2013) 196-207.
[39] P. Fede, O. Simonin, P. Villedieu, Monte-Carlo simulation of colliding particles or coalescing droplets transported by a turbulent flow in the framework of a joint fluid-particle pdf approach, Int. J. Multiph. Flow 74(2015) 165-183.
[40] E. Debry, B. Sportisse, B. Jourdain, A stochastic approach for the numerical simulation of the general dynamics equation for aerosols, J. Comput. Phys. 184(2003) 649-669.
[41] D.L. Marchisio, R.O. Fox, Solution of population balance equations using the direct quadrature method of moments, J. Aerosol Sci. 36(2005) 43-73.
[42] M.Z. Yu, J.Z. Lin, T.L. Chan, A new moment method for solving the coagulation equation for particles in Brownian motion, Aerosol Sci. Technol. 42(2008) 705-713.
[43] M. Balthasar, M. Frenklach, 2005. Detailed kinetic modeling of soot aggregate formation in laminar premixed flames, Combust. Flame 40(2005) 130-145.
[44] M.Z. Yu, T.L. Chan, A bimodal moment method model for submicron fractal-like agglomerates undergoing Brownian coagulation, J. Aerosol Sci. 88(2015) 19-34.
[45] M.Z. Yu, X. Zhang, G. Jin, J. Lin, M. Seipenbusch, A new analytical solution for solving the population balance equation in the continuum-slip regime, J. Aerosol Sci. 80(2015) 1-10.
[46] M. Kostoglou, A.G. Konstandopoulos, Evolution of aggregate size and fractal dimension during Brownian coagulation, J. Aerosol Sci. 32(2001) 1399-1420.
[47] M. Yu, Y. Liu, J. Lin, M. Seipenbusch, Generalized TEMOM scheme for solving the population balance equation, Aerosol Sci. Technol. 49(2015), 1021-1036.
[48] M.Z. Yu, Y. Liu, G. Jin, H. Jin, A new analytical solution for agglomerate growth undergoing Brownian coagulation, Appl. Math. Model. 40(2016) 5497-5509.
[49] Z. Jiang, J. Shen, Z. Lu, Bivariate Taylor-series expansion method of moment for particle population balance equation in Brownian coagulation, J. Aerosol Sci. 114(2017) 94-106.
[50] I. Pesmazoglou, A.M. Kempf, S. Navarro-Martinez, Large eddy simulation of particle aggregation in turbulent jets, J. Aerosol Sci. 111(2017) 1-17.
[51] M.Z. Yu, J.Z. Lin, T.L. Chan, Numerical simulation for nucleated vehicle exhaust particulate matters via the TEMOM/LES method. Int. J. Mod. Phys. C 20(2009) 399-421.
[52] S. di Stasio, A.G. Konstandopoulos, M. Kostoglou, Cluster-cluster aggregation kinetics and primary particle growth of soot nanoparticles in flame by light scattering and numerical simulations, J. Colloid Interface Sci. 247(2002) 33-46.
[53] H. Watanabe, R. Kurose, M. Hayashi, T. Kitano, S. Komori, Effects of ambient pressure and precursors on soot formation in spray flames, Adv. Powder Technol. 25(2014) 1376-1387.

[54] K.W. Lee, Y.J. Lee, D.S. Han, The log-normal size distribution theory for Brownian coagulation in the low Knudsen number regime, J. Colloid Interface Sci. 188(1997) 486-492.
[55] M.Z. Yu, J.Z. Lin, Taylor-expansion moment method for agglomerate coagulation due to Brownian motion in the entire size regime, J. Colloid Interface Sci. 336(2009) 142-149.
[56] I.M. Kennedy, S.J. Harris, Direct numerical simulation of aerosol coagulation with van der Waals forces, J. Colloid Interface Sci. 130(1989) 489-497.
[57] N.A. Fuchs, The Mechanics of Aerosols. Pergamon Press, New York, 1964.
[58] A. Kazakov, M. Frenklach, Dynamic modeling of soot particle coagulation and aggregation: implementation with the method of moments and application to high-pressure laminar premixed flames, Combust. Flame 114(1998) 484-501.
[59] M. Frenklach, H. Wang, In Soot Formation in Combustion: Mechanisms and Models (H. Bockhorn, Ed.), Springer-Verlag, Berlin, 1994, pp. 165–190.
[60] A. Kazakov, H. Wang, M. Frenklach, Detailed modeling of soot formation in laminar premixed ethylene flames at a pressure of 10 bar, Combust. Flame 100(1995) 111-120.
[61] F.E. Kruis, K.A. Kusters, S.E. Pratsinis, B. Scarlett, A simple model for the evolution of the characteristics of aggregate particles undergoing coagulation and sintering, Aerosol Sci. Technol. 19(1993) 514-526.
[62] S.M. Mahmoud, G.J. Nathan, Z.T. Alwahabi, Z.W. Sun, P.R. Medwell, B.B. Dally, The effect of exit Reynolds number on soot volume fraction in turbulent non-premixed jet flames, Combust. Flame 187(2018) 42-51.

List of Figures

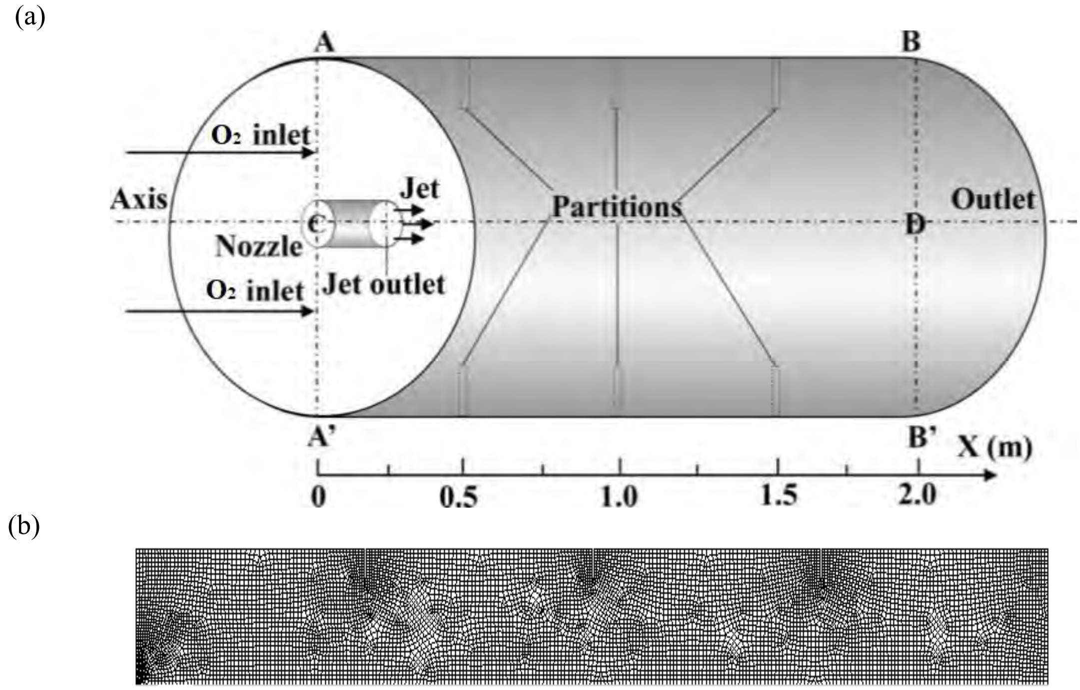

Fig. 1. Schematic configuration of the cylindrical combustor [29]: (a) Three-dimensional combustor; (b) two-dimensional axisymmetric grid mesh.

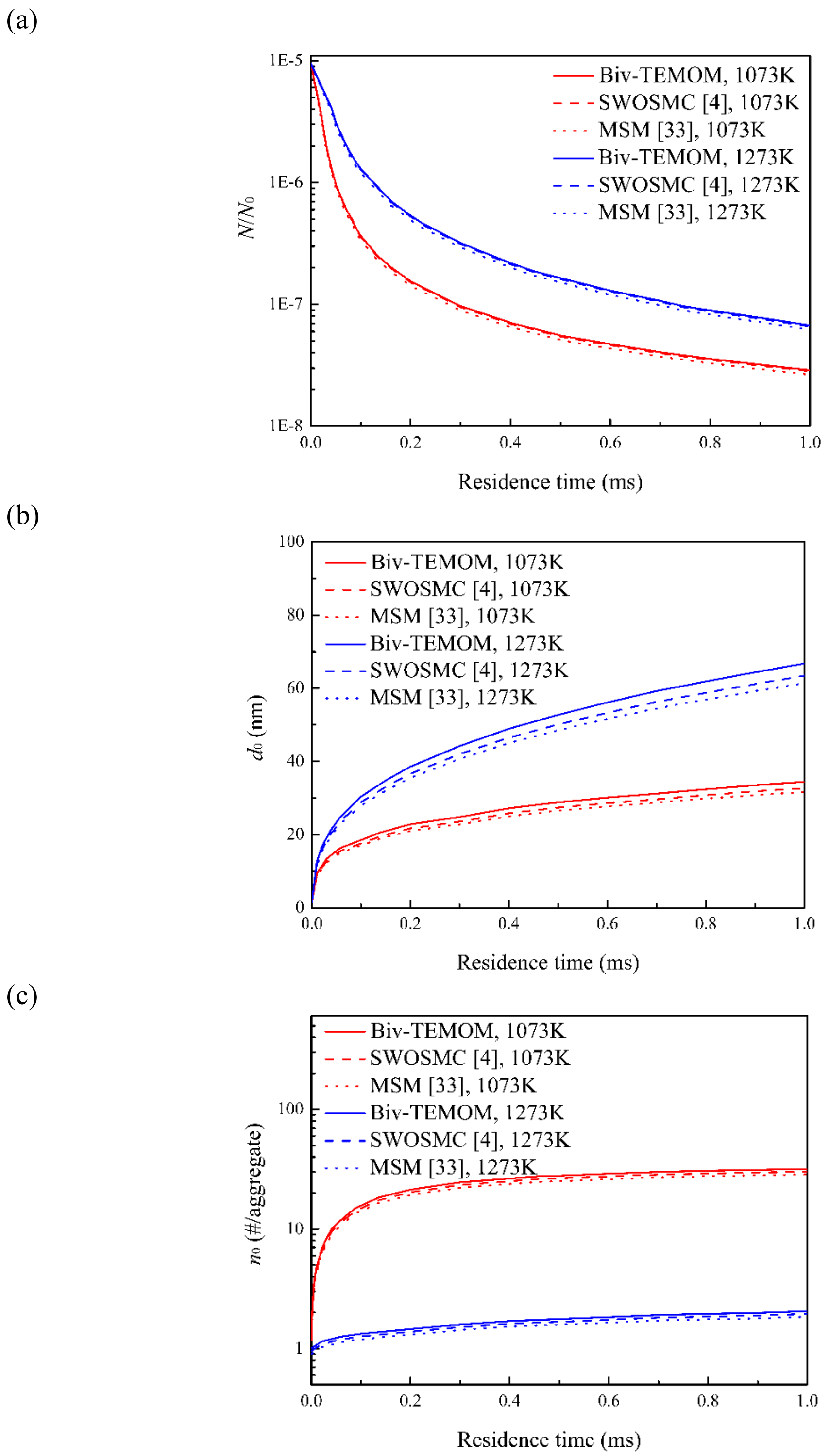

Fig. 2. Bivariate Taylor expansion method of moments (Biv-TEMOM) model validation with the stochastically weighted operator splitting Monte Carlo (SWOSMC) method [4] and the moving sectional method (MSM) [33]: (a) non-dimensional total number density of aggregate particles; (b) mean diameter of primary particles; and (c) mean number of primary particles per aggregate.

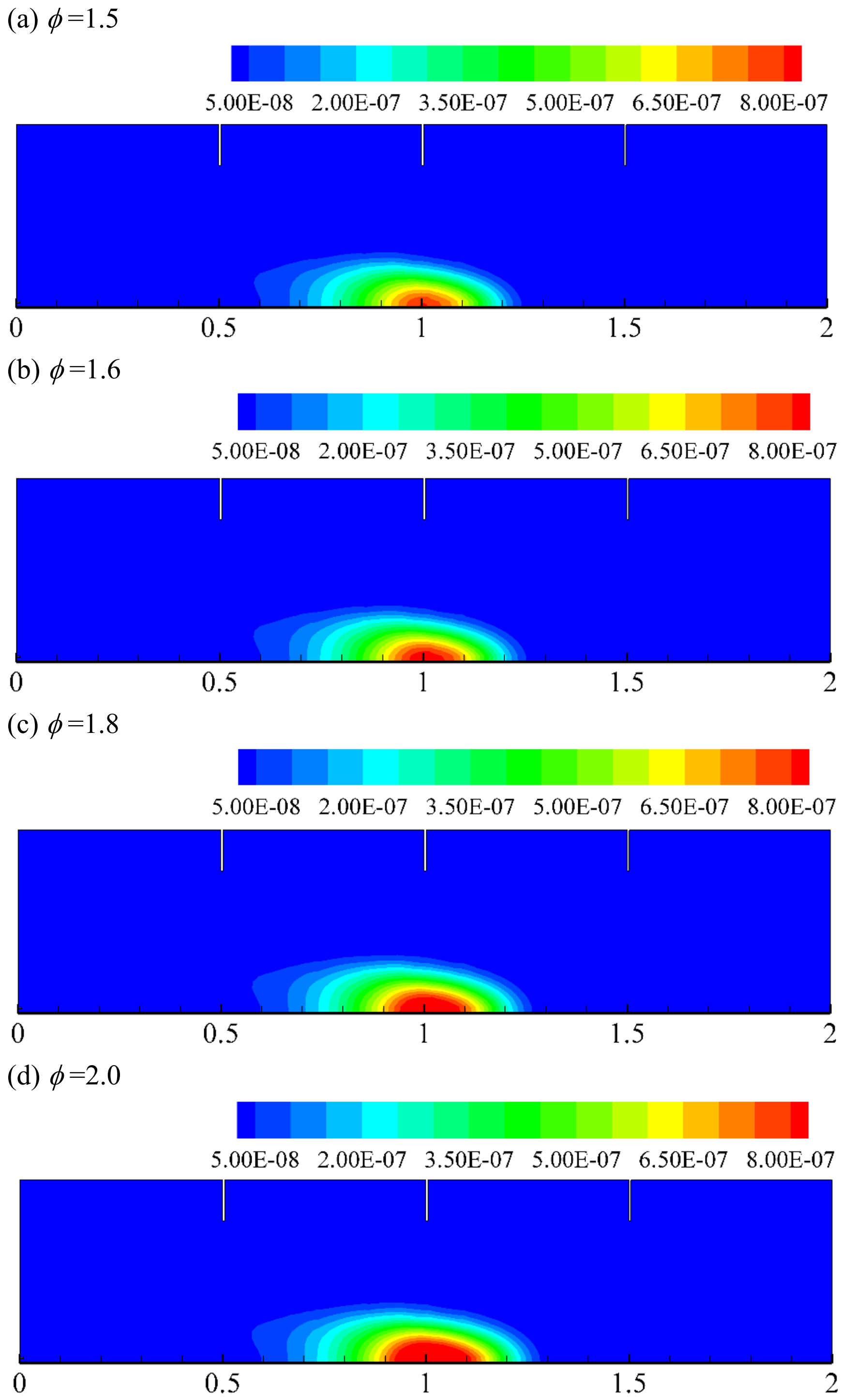

Fig. 3. The total soot volume fraction (m^3/m^3) distributions along the axial distance (m) at Re_j = 36,000.

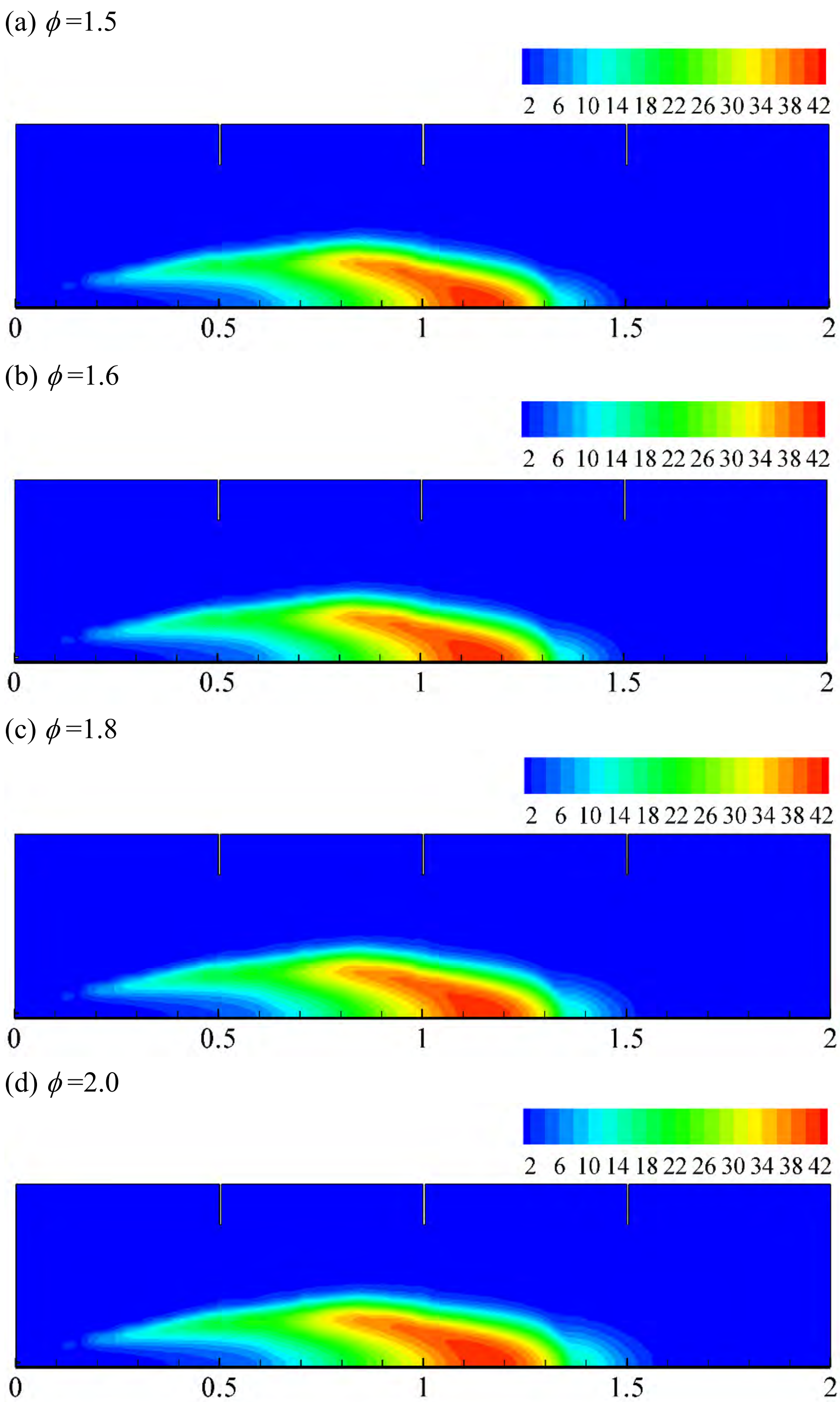

Fig. 4. The soot coagulation rate ($\times10^{18}$ #/m^3/s) distributions along the axial distance (m) at Re_j = 36,000.

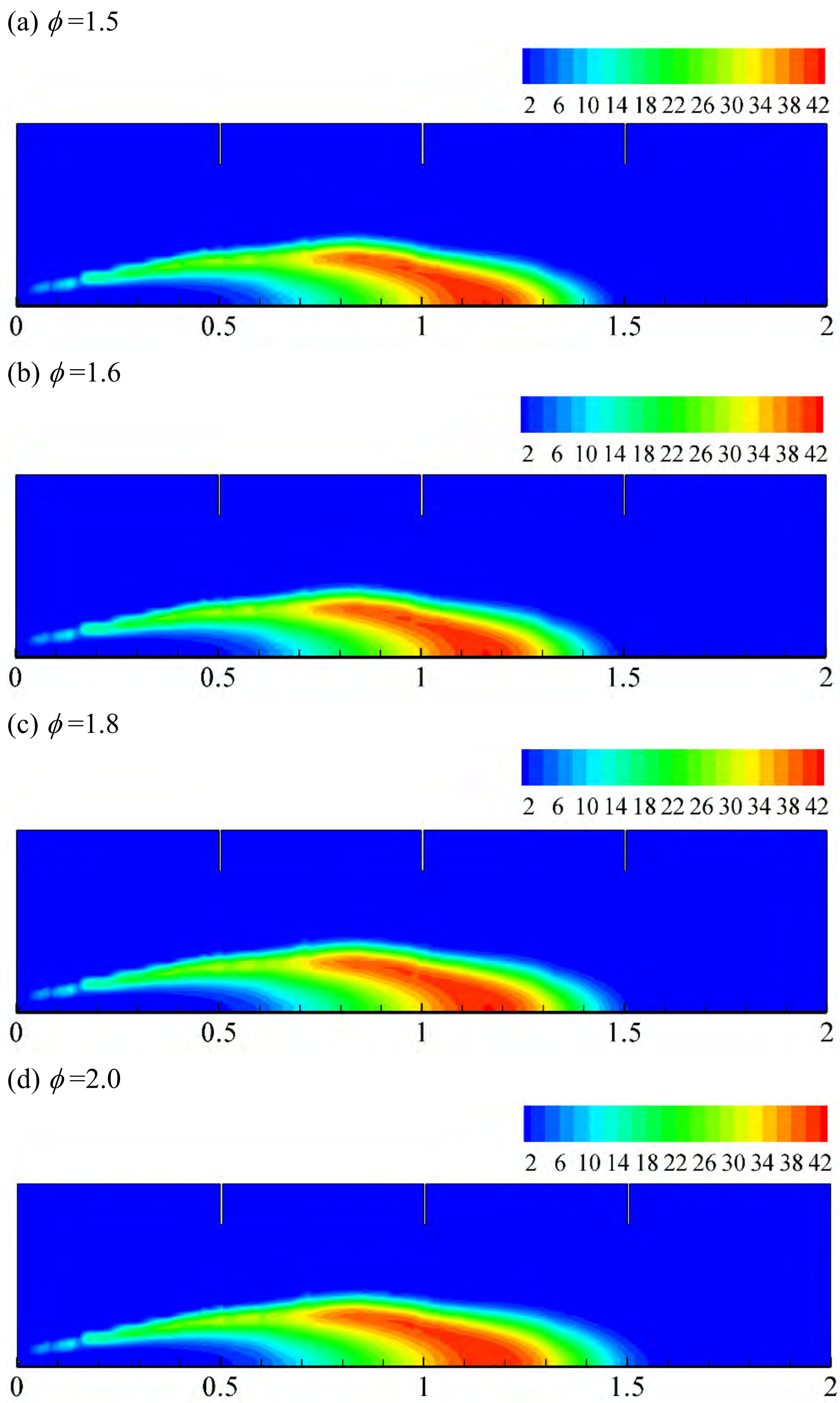

Fig. 5. The soot nucleation rate ($\times 10^{18}$ #/m^3/s) distributions along the axial distance (m) at $Re_j = 36{,}000$.

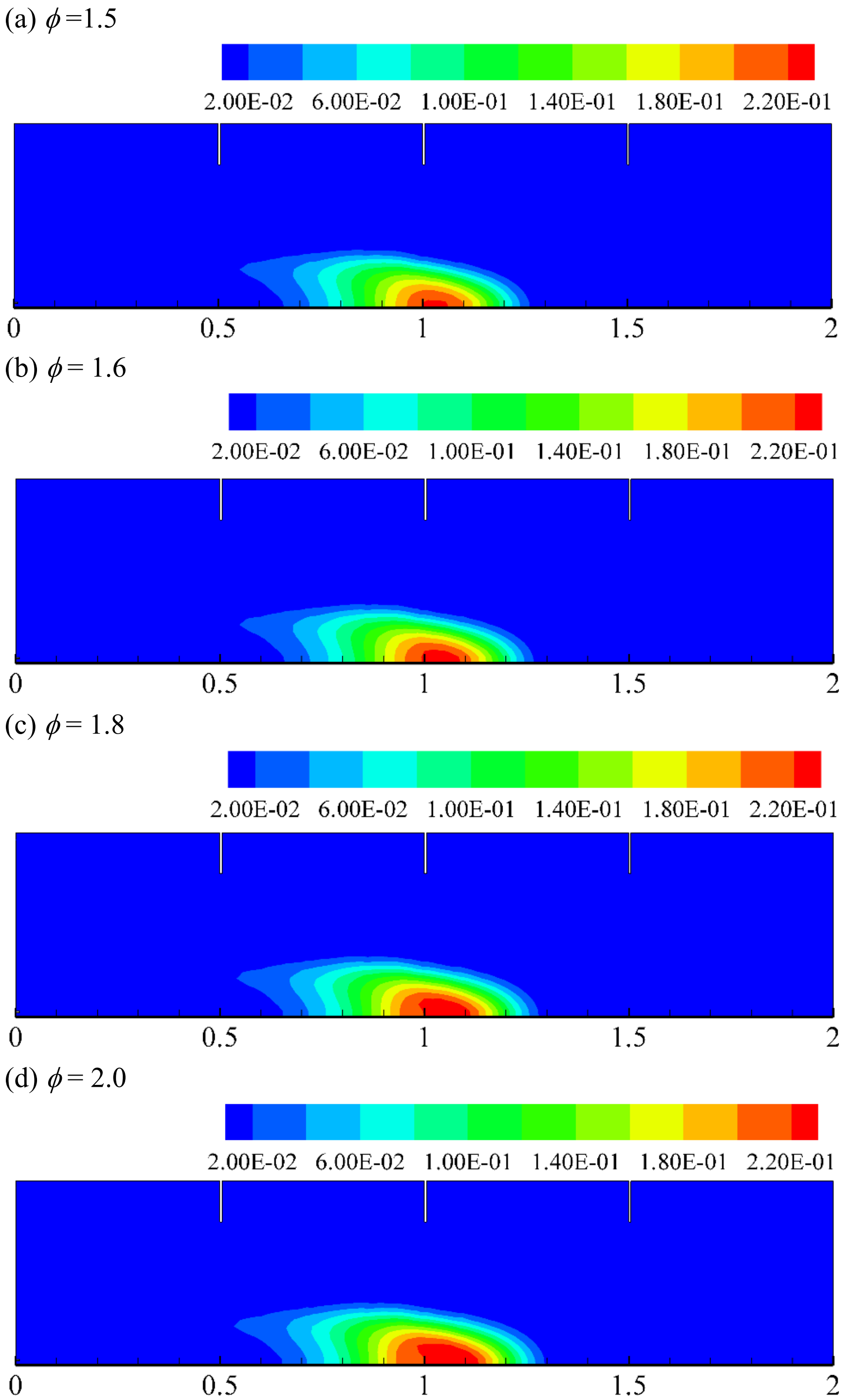

Fig. 6. The soot surface growth rate (kg/m^3/s) distributions along the axial distance (m) at Re_j = 36,000.

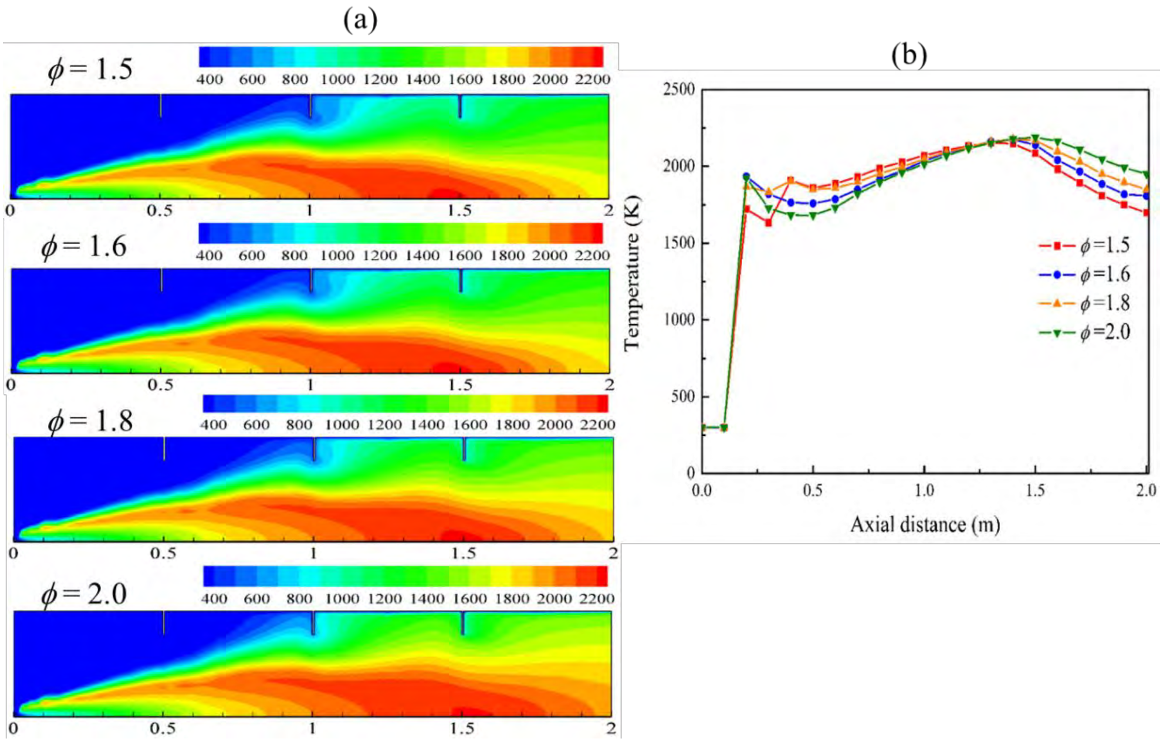

Fig. 7. The effect of equivalence ratio, ϕ on flame temperature (K) at Re_j= 36,000: (a) flame temperature distributions and (b) flame temperatures along the axial distance (m) at radial distance, y = 0.05 m.

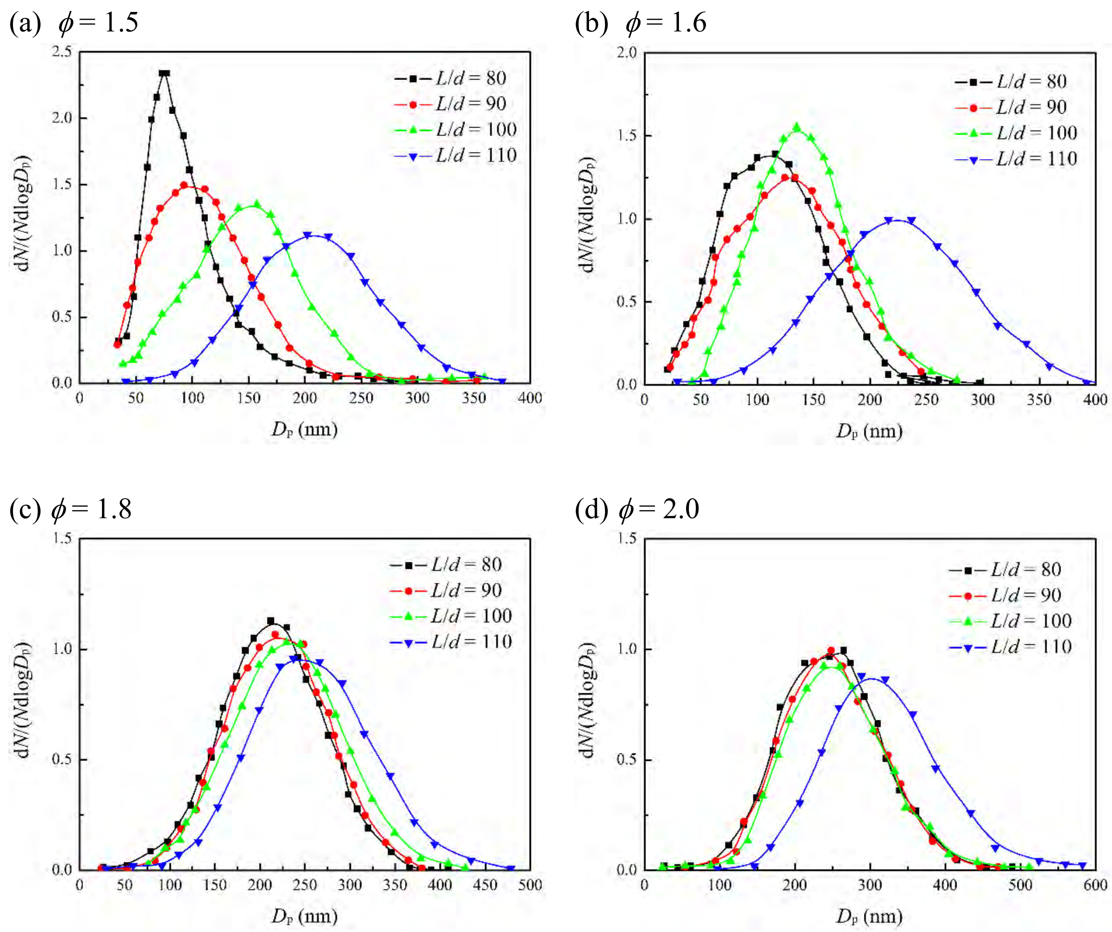

Fig. 8. The normalized particle size distributions of soot aggregates for different equivalence ratios, ϕ and L/d at $Re_j = 36{,}000$.

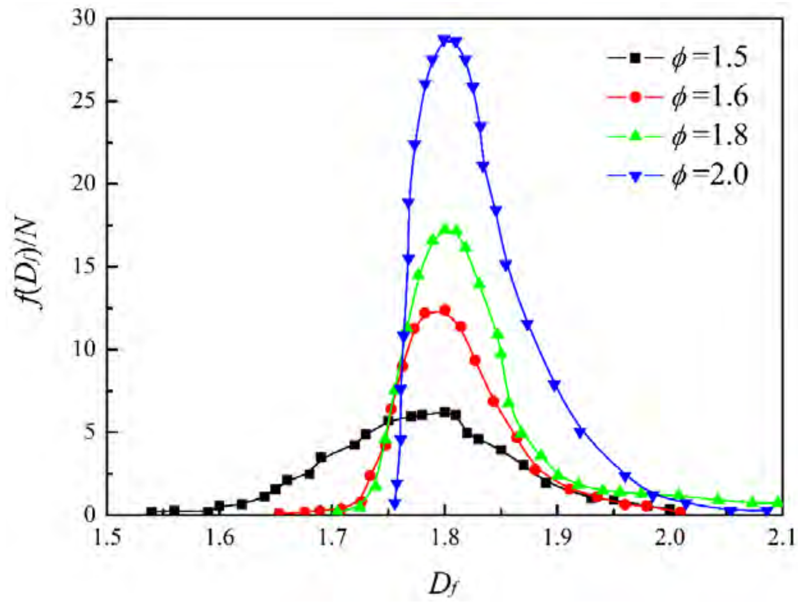

Fig. 9. The normalized fractal dimension distributions of soot aggregates for different equivalence ratios, ϕ at $Re_j = 36{,}000$.

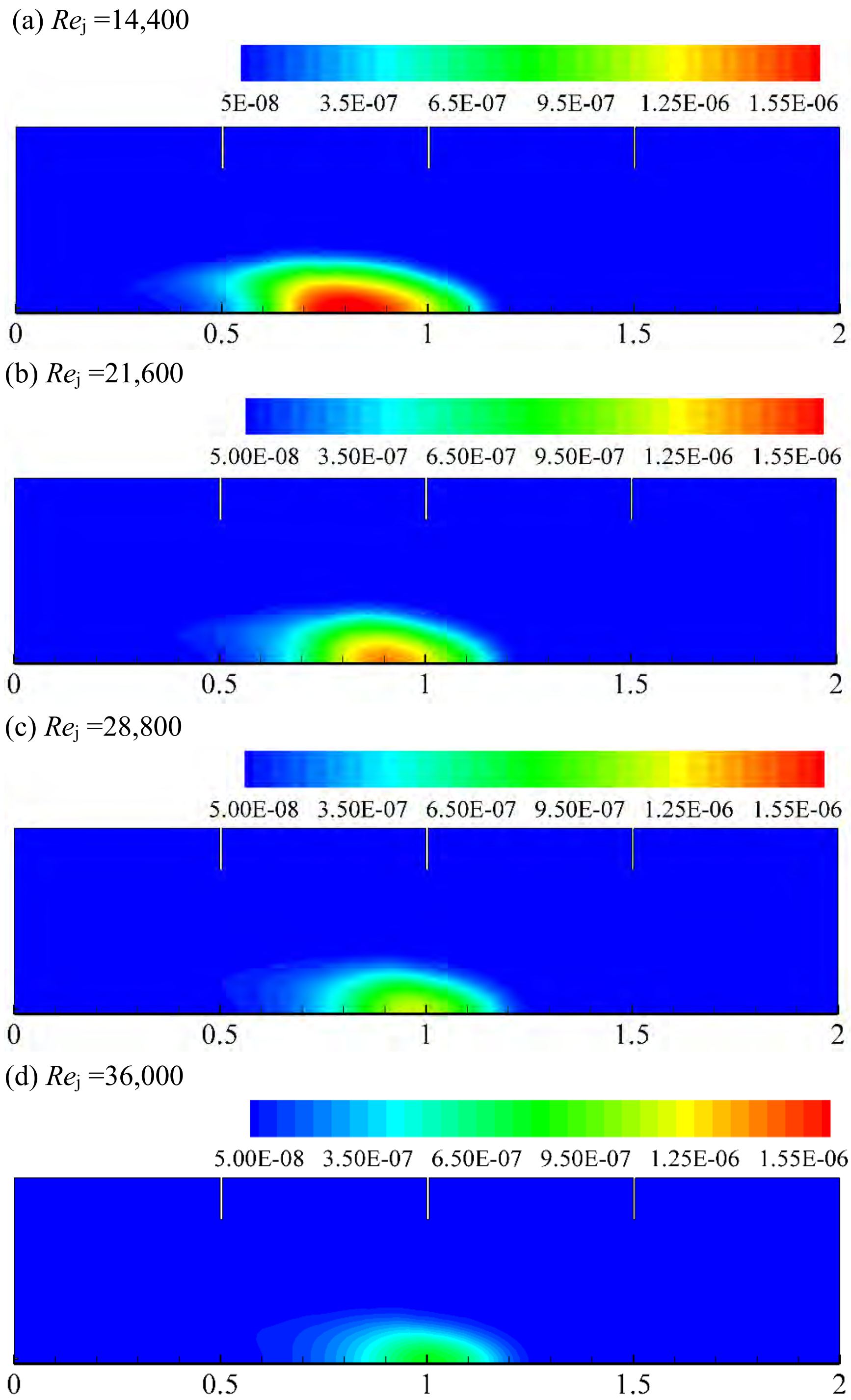

Fig. 10. The total soot volume fraction (m^3/m^3) distributions along the axial distance (m) at $\phi = 1.5$.

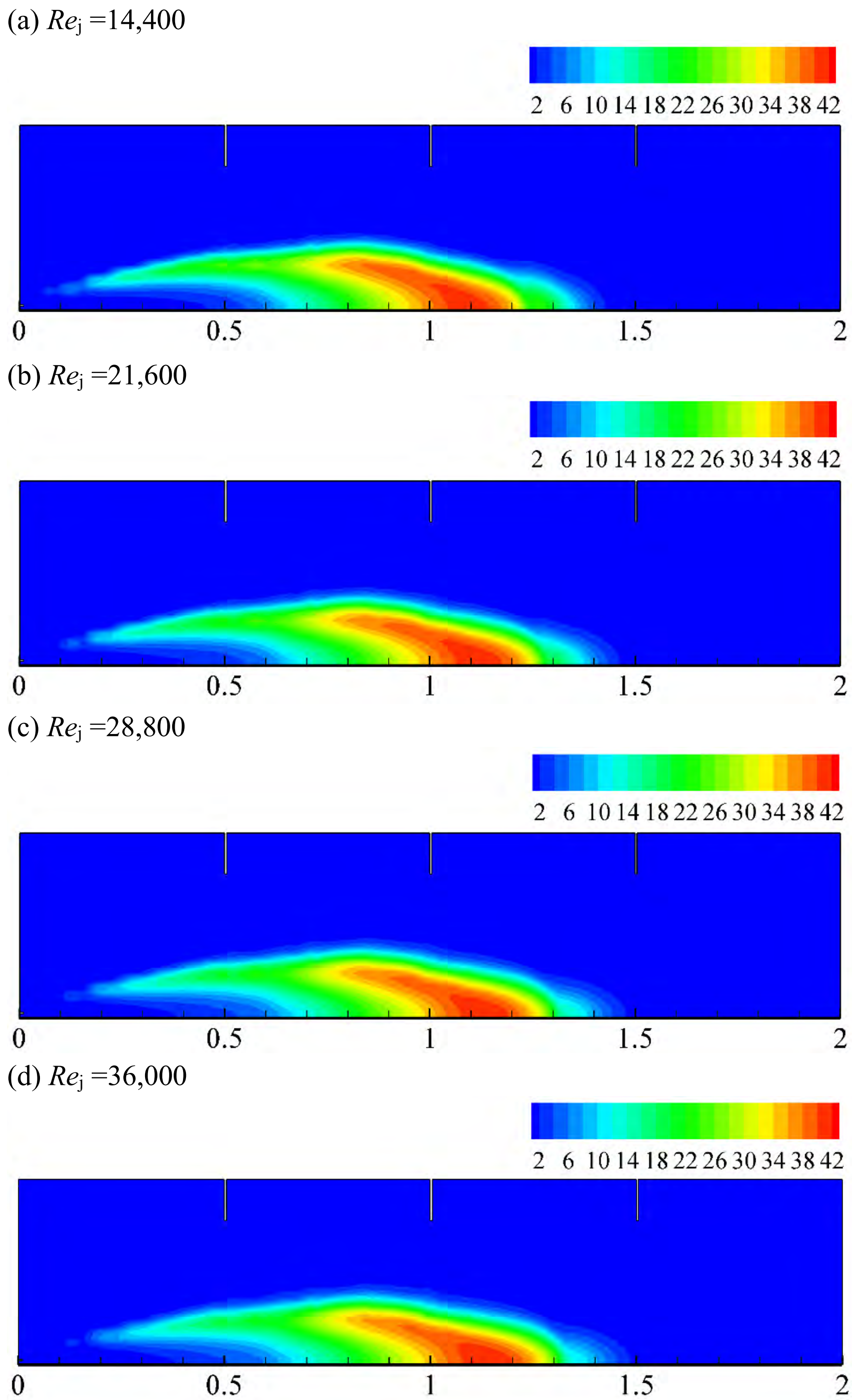

Fig. 11. The soot coagulation rate ($\times 10^{18}$ #/m^3/s) distributions along the axial distance (m) at $\phi = 1.5$.

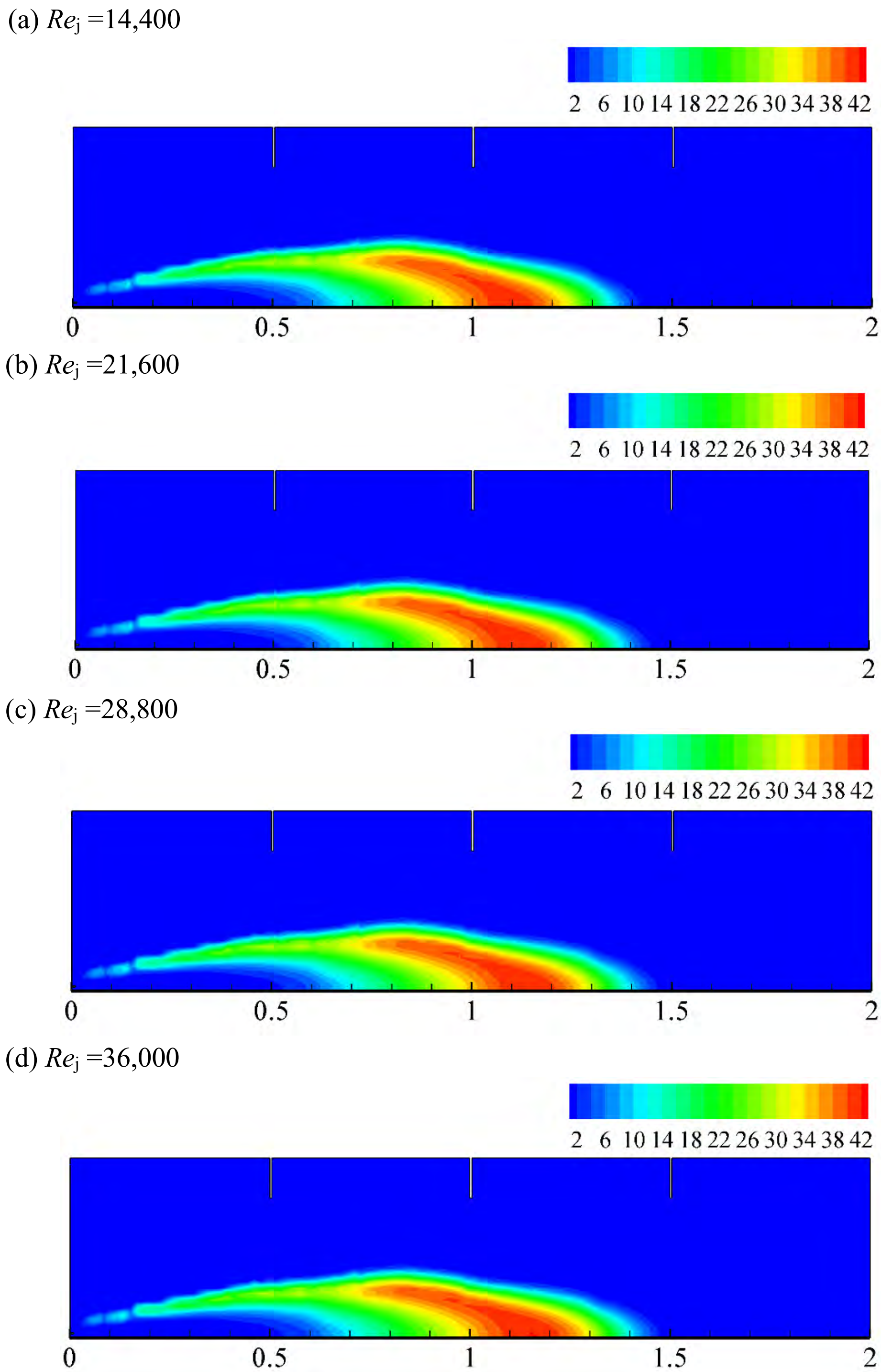

Fig. 12. The soot nucleation rate ($\times 10^{18}$ #/m^3/s) distributions along the axial distance (m) at $\phi = 1.5$.

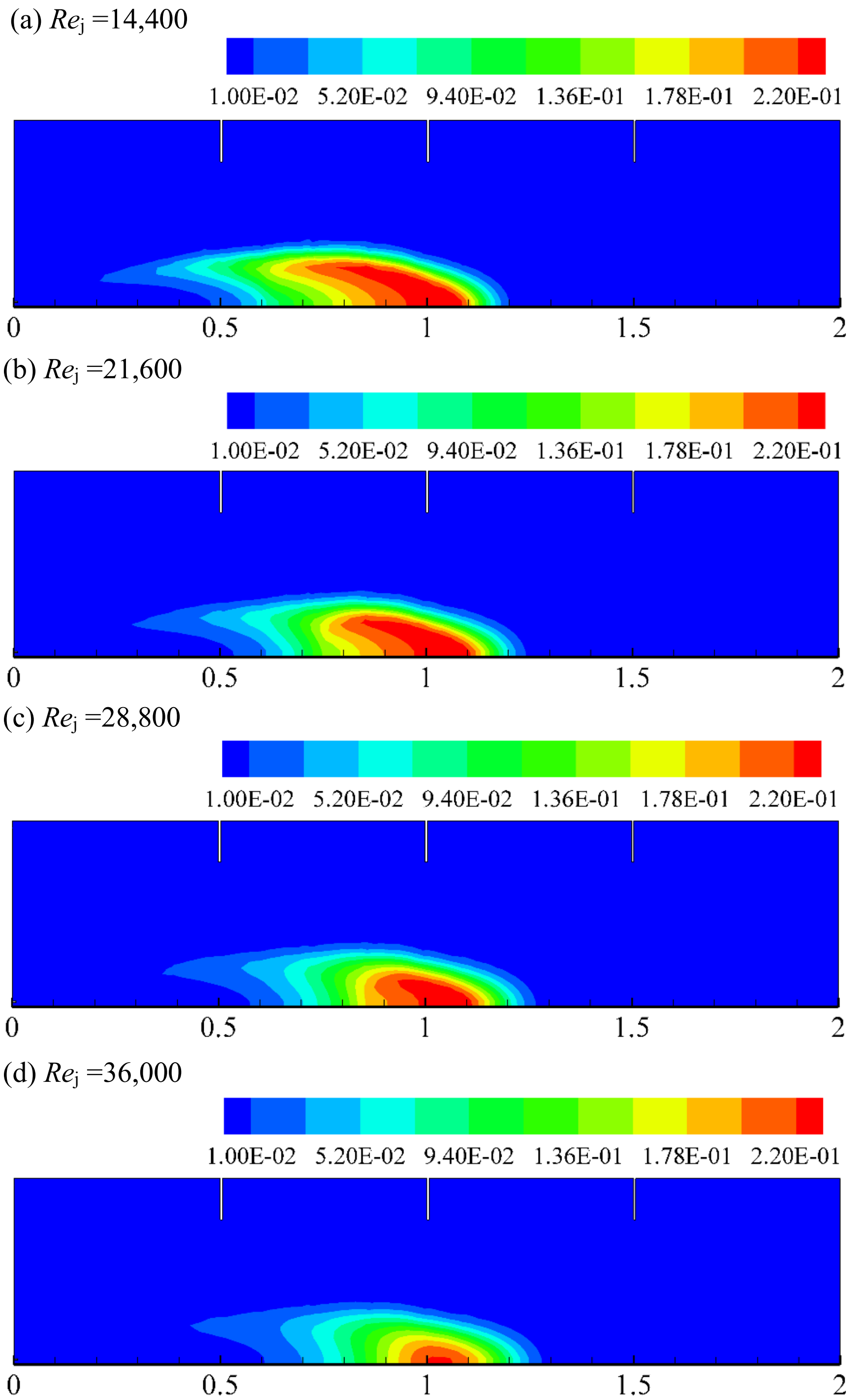

Fig. 13. The soot surface growth rate (kg/m^3/s) distributions along the axial distance (m) at $\phi = 1.5$.

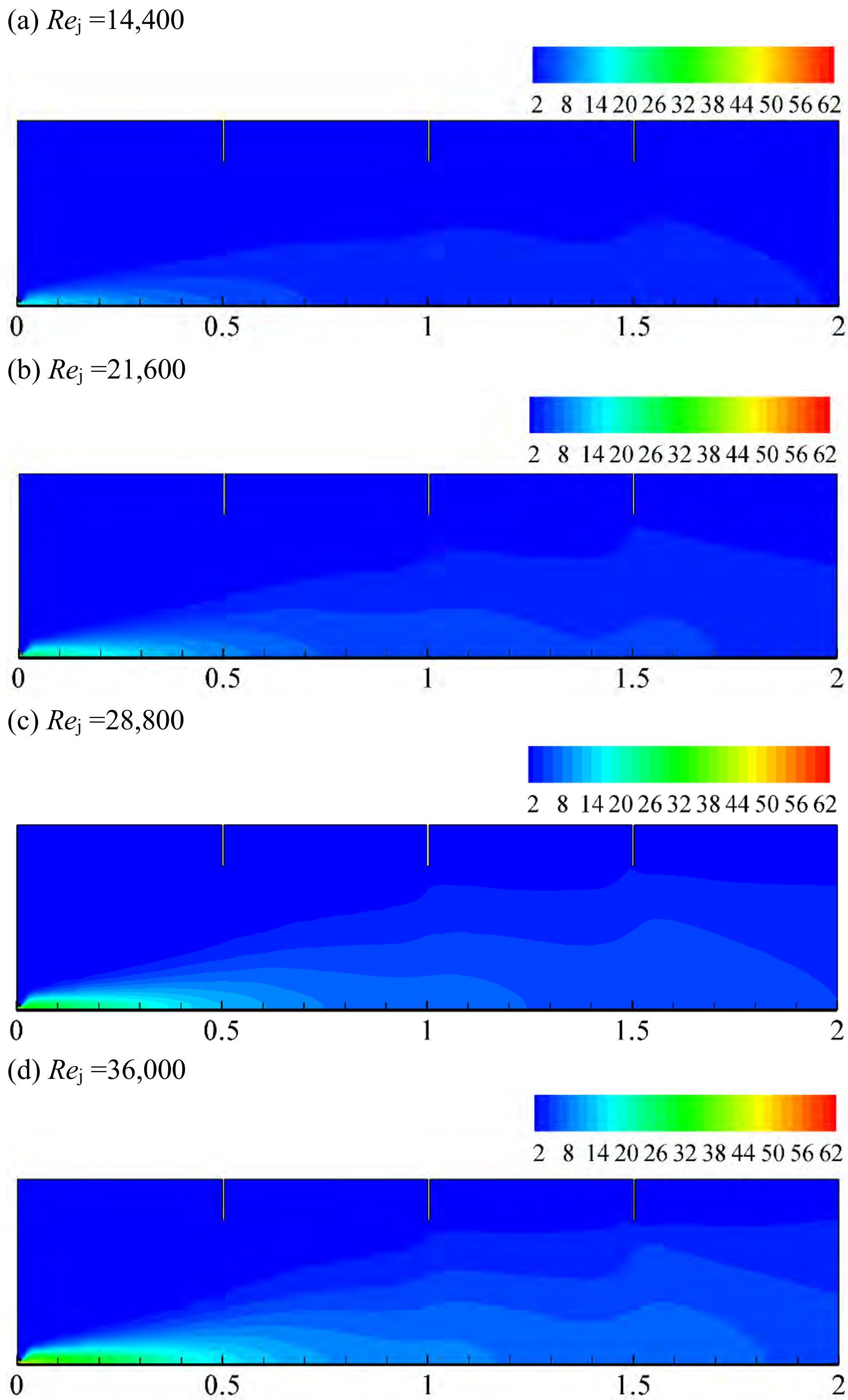

Fig. 14. The flame jet velocity (m/s) distributions along the axial distance (m) at $\phi = 1.5$.

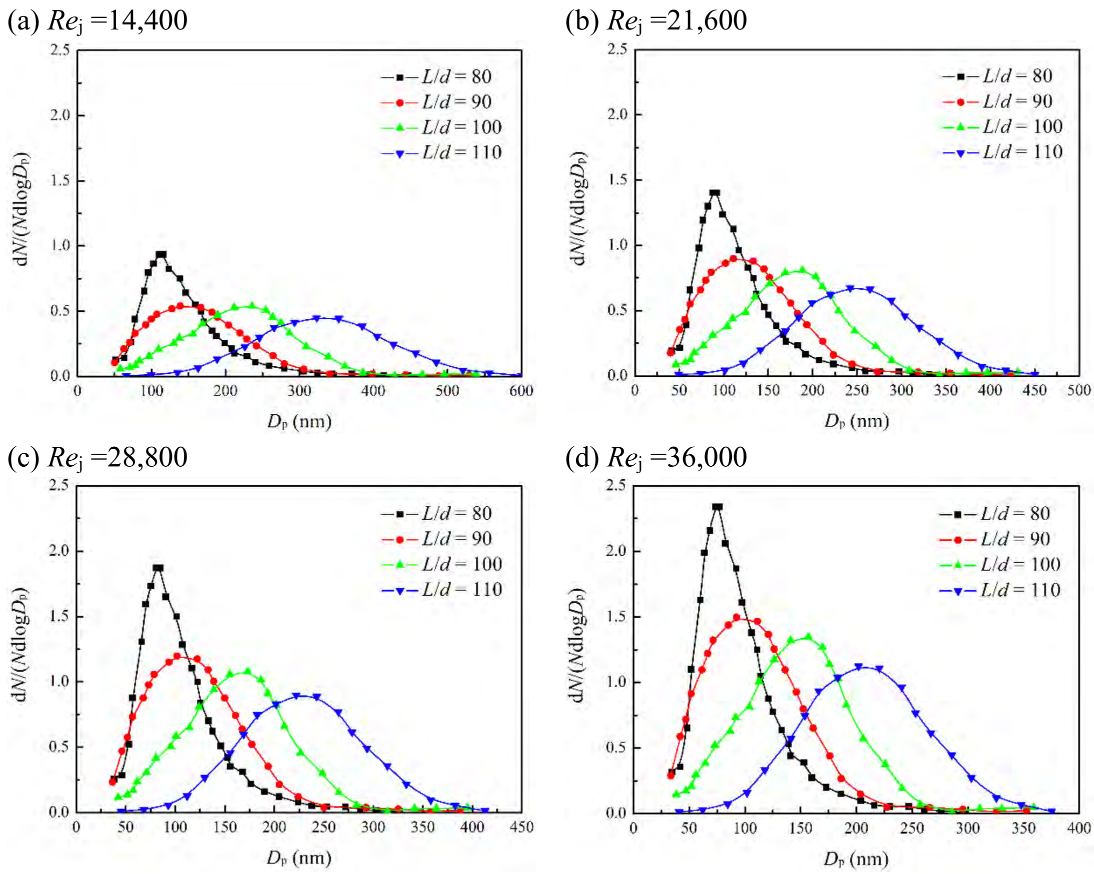

Fig. 15. The normalized particle size distributions of soot aggregates for different Re_j at ϕ= 1.5.

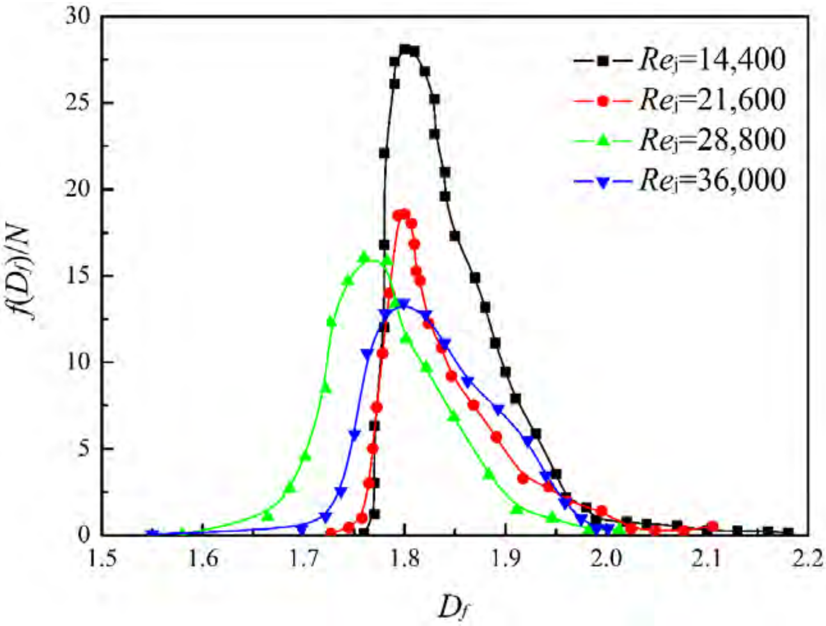

Fig. 16. The normalized fractal dimension distributions of soot aggregates for different Re_j at $\phi = 1.5$.

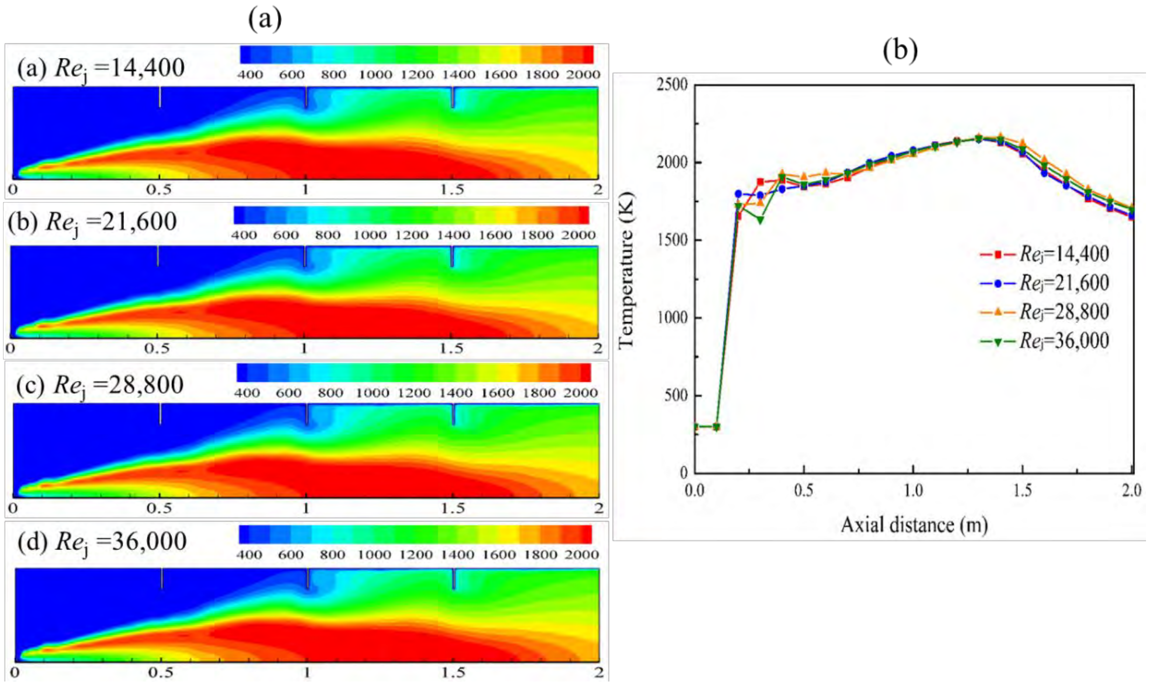

Fig. 17. The effect of jet Reynolds number, Re_j on flame temperature (K) at ϕ= 1.5: (a) flame temperature distributions (m) and (b) flame temperatures along the axial distance (m) at radial distance, y = 0.05 m.

List of Tables

Table. 1. Initial conditions for the numerical model validation [61].

Parameters	Values
Initial particle number concentration	3.6212×10^{27} #/m^3
Initial particle diameter	3.3689×10^{-10} m
Primary particle density	2.33×10^{27} kg/m^3
Pressure	101.325 kPa
Fractal dimension of aggregate	1.8
Flame temperatures	1073K and 1273K

Table. 2. Simulated cases of the turbulent ethylene-oxygen flame.

Cases	Inlet jet flow velocity (m/s)	Jet Reynolds number, Re_j	Equivalence ratio, ϕ
1	60	36,000	1.5
2	60	36,000	1.6
3	60	36,000	1.8
4	60	36,000	2.0
5	24	14,400	1.5
6	36	21,600	1.5
7	48	28,800	1.5